

## Article

# Responses of a Modular Floating Wind TLP of MarsVAWT Supporting a 10 MW Vertical Axis Wind Turbine

Sung Youn Boo <sup>1,\*</sup>, Steffen Allan Shelley <sup>1</sup>, D. Todd Griffith <sup>2</sup>  and Alejandra S. Escalera Mendoza <sup>2</sup> <sup>1</sup> VL Offshore, LLC, Houston, TX 77084, USA<sup>2</sup> Department of Mechanical Engineering, The University of Texas at Dallas, Richardson, TX 75080, USA

\* Correspondence: sboo@vloffshore.com

**Abstract:** Offshore floating wind foundations supporting a large wind turbine require a large yard facility or significant facility upgrades for their fabrication. To overcome the cost increase associated with facility upgrades, an innovative lightweight modular floating foundation is developed. The foundation comprises multiple modules to enable their assembly on water, offering many benefits and expanding fabrication options for a reduction in the overall cost of the platform. In this paper, the foundation modules and their assembly are briefly described, and an analysis of the platform's dynamic responses is presented. The modular foundation includes a modular and lightweight tension leg platform (TLP) called "MarsVAWT" which supports a Darrieus 10 MW vertical axis wind turbine (VAWT). The platform is moored with highly pretensioned wire rope tendons. The responses of the platform are analyzed in the time domain in a semi-coupled manner under the turbine operating and parked conditions for an offshore site in the US Northeast. The tower base shear forces and bending moments increase considerably with the combination of wind and waves, compared to those with wind only. The tendon tensions on the weatherside in the operating condition at high wind speeds are comparable to the values of the 50-year extreme (parked). The tendon tension increases are highly correlated to the platform pitch, as well as the horizontal and vertical velocities and vertical acceleration at the tendon porch. The modular platform performances and tendon designs are confirmed to comply with industry standards and practices.

**Keywords:** TLP; VAWT; floating offshore wind turbine; MarsVAWT; Mars-Wind; modular; tendon



**Citation:** Boo, S.Y.; Shelley, S.A.; Griffith, D.T.; Escalera Mendoza, A.S. Responses of a Modular Floating Wind TLP of MarsVAWT Supporting a 10 MW Vertical Axis Wind Turbine. *Wind* **2023**, *3*, 513–544. <https://doi.org/10.3390/wind3040029>

Academic Editor: Yingyi Liu

Received: 10 September 2023

Revised: 18 October 2023

Accepted: 1 November 2023

Published: 6 November 2023



**Copyright:** © 2023 by the authors. Licensee MDPI, Basel, Switzerland. This article is an open access article distributed under the terms and conditions of the Creative Commons Attribution (CC BY) license (<https://creativecommons.org/licenses/by/4.0/>).

## 1. Introduction

There are two representative types of wind turbines differentiated by the axis of the rotor's rotation: a vertical axis wind turbine and a horizontal axis wind turbine (HAWT). There have been significant technical research and development in the HAWT system and floating foundations to support a single unit of a HAWT [1–4] and multiple units of turbines [5,6]. There have also been commercial deployments of floating offshore platforms with HAWTs, including a spar with 6 MW [7] and semi-submersible with 8.4 MW [8].

Arredondo-Galeana [9] states that the technology readiness level (TRL) of the floating VAWT platform is much lower than that of the HAWT, especially in terms of the power take-off and full system for a large VAWT, although there has been progress in VAWT development for land and floating offshore applications [10,11]. However, offshore floating VAWTs have several advantages over floating HAWTs. The VAWT system's mass center is lower due to the position of the generator [12]. This feature can improve the hydrostatic stability of the platform, offering the possibility of a smaller floating foundation design. The turbine generator can be housed inside a foundation structure below the tower base, which provides easier access for maintenance. A VAWT turbine's load center is typically located at a height lower than that of a HAWT's thrust center, resulting in lower heeling moments to the platform. Power generation variations in VAWTs are small even at higher platform heel angles, which eventually allows for the relaxation of the maximum (or mean)

platform pitch angle restriction on HAWT platforms. A recent study with a helical VAWT shows that the turbulence that induced load fluctuations on the helical VAWT may be significantly reduced [13], which may be beneficial to the platform motion and mooring fatigue performances. To take advantage of VAWTs' characteristics, the floating foundation size may be reduced. As for the turbine spacing, a study suggests that VAWT platforms can be spaced closer in the downstream direction between four and eight rotor diameters as the wake is recovered relatively quickly [9,13,14]. HAWT spacing is, on the other hand, typically eight to ten rotor diameters [9]. The closer deployment of a floating VAWT can increase the wind farm power density and space utilization [13], while also reducing the length of inter-platform power cables required in a wind farm, resulting in cable cost savings.

However, there are some unique engineering challenges involved in the platform design with VAWTs. VAWT platform designs need to deal with the cyclic turbine loads of the thrust, lateral (side-to-side) force, and torque [15] acting at the aerodynamic pressure center (PC) as depicted in Figure 1. The thrust increases with the wind until the wind speeds reach the cut-out wind speed. Thus, maximum VAWT loadings likely occur at the cut-out wind speed rather than the rated wind speed [16,17] as seen in HAWTs. The lateral force generates the platform's horizontal and rotational motion, while the torque causes the platform yaw. The parked blade drag of the VAWT increases the platform heeling moment because the blades typically do not include a pitch control. There has been an effort to implement active blade control for a 6 MW H-rotor VAWT, presenting a reduction in the VAWT wind loading during the parked condition and resulting in a lighter floater design [18]. These imply the complexity of the aero-hydrodynamic couplings between the VAWT and floater during the turbine's operation and extreme parked conditions, suggesting the design's governing condition should be identified considering all possible scenarios.

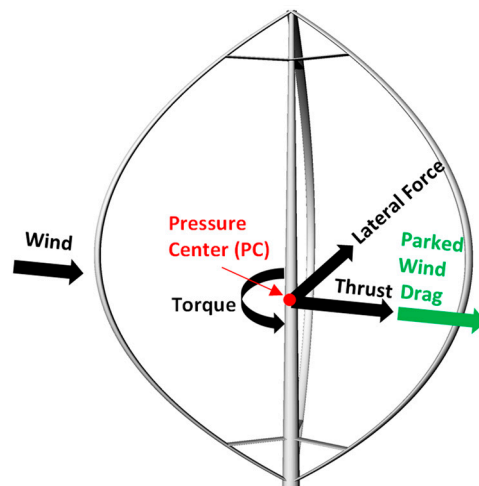


**Figure 1.** Turbine forces and moments of a Darrieus-type VAWT.

For VAWT platforms, there are primarily three different floating hull (foundation) types originating from oil and gas platforms: the spar-type mono-hull cylinder, semi-submersible, and TLP. A spar platform has a low yaw stiffness and may present a tendency for high-yaw motion induced by the VAWT turbine torque at a high wind speed. A mean yaw motion is reported to be about seven degrees at the cut-out wind speed with a 5 MW two-bladed Darrieus VAWT on a spar [19]. The yaw motion with a similar magnitude is also observed in a semi-submersible with a 6 MW VAWT under a survival condition [18]. The spar yaw stiffness can be improved by increasing the fairlead radius (or increasing the diameter of the spar) or adding more mooring lines, which involves greater mooring system costs [20]. Based on a small-scale test of the SeaTwirl of the H-rotor type, a commercial-scale spar platform with 1 MW is planned to be built and deployed at a minimum water depth of 100 m [21].

Like the spar, a semi-submersible floater is widely used to accommodate VAWTs. A fully coupled analysis was performed with a DeepWind rotor of 5 MW integrated to a

semi-submersible [22,23]. The floater was the DeepWind semi-submersible from the OC4 project [24]. Also, a Tri-Floater semi-submersible was utilized to support an H-rotor-type VAWT rated at 6 MW [18]. It showed a weight reduction of 20% from a HAWT of the same rated power, associated with the wind load reduction using blade control. The present work also closely investigates the wind loads induced by the parked blades during extreme parked conditions. An additional semi-submersible design is the VertiWind mounted on a four-column semi-submersible with truss members [25].

Studies on TLP floaters with VAWTs are few, but there is rather active research on TLPs with HAWTs such as the mono-column TLP [26–28] and multi-column TLP [29–31]. Boo [29] proposed a four-column TLP with a 6 MW HAWT and demonstrated its technical feasibility at an ultra-deep-water site of 1000 m located offshore of Hawaii. The majority of TLP floaters with HAWTs or VAWTs have a mono-column floater with long yoke structures to connect the tendons. Borg [32] also considers a mono-column TLP for a DeepWind H-rotor VAWT of 5 MW to assess the dominant load on the platform and address the TLP tendon snap loading that may occur by the tendon slack in extreme conditions. A recent study for a floating VAWT adopted a 5 MW Darrieus VAWT mounted on a multi-column TLP to develop a semi-coupled simulation tool with seven-degree of freedom (7-DoF) [16]. The limited work on TLPs compared to other platforms may be due to TLPs' complex characteristics that are quite different from those of spars or semi-submersibles, or to the fact that no representative TLP designs are available for researchers.

A new design of a TLP for floating wind incorporates our prior experience of dealing with key design drivers, e.g., the hull steel weight and many others, as described in the next section. Therefore, this TLP design needs to be completed in an iterative manner from the initial design to installation of the platform to comply with the design requirements. The floating TLP in the present work considers all the design iterations and processes to reach a target and is briefly described in this paper.

As described, most studies on TLPs supporting VAWTs or HAWTs consider mono-column floaters inherently lacking self-stability without tendon connections or additional supporting vessels. This complicates the tow of the TLP with the integrated turbine and thus increases the associated cost and risk. To avoid a complex pre-service operation, the new TLP in the present work is designed with a multi-column hull to provide sufficient stability to allow for towing out from the quayside using a conventional towing vessel. The existing TLPs for VAWTs or HAWTs are designed for relatively small turbines with a rated power of 6 MW or lower. However, when the turbine becomes larger, e.g., 10+ MW, the overall spans of the floater also become very large, which may exceed a fabrication yard's capacity in terms of space and equipment. This drawback must be resolved to lower the platform's cost by, for instance, implementing the modularized floater assembly concept or other methods.

Therefore, the objective of the present work is to (1) develop a new lightweight and self-stable modular TLP floating foundation (MarsVAWT) to support a 10 MW Darrieus VAWT; (2) evaluate the dynamic responses of the modular TLP to characterize the TLP with the VAWT for upscaling; and (3) confirm that the design complies with industry design standards.

The response simulation is conducted in the time domain using a semi-coupled method, in which the turbine's loads of thrust, lateral force, and torque are input as external loads with time histories. The turbine blades and tower are modelled differently. The tower is modeled with the finite element method (FEM) using the original tower design, but the blades are lumped into two masses and distributed on the tower. In the numerical model, the lumped blade moments of inertias are iteratively determined until the turbine responses converge closely to those of the original design.

The simulation is carried out for the turbine's operation and the 50-year extreme (parked) conditions. The steady inflow wind is used in producing the VAWT aerodynamic loads for the operating condition, while the Norwegian Petroleum Directorate (NPD) wind spectrum is used for the 50-year extreme parked condition. The response analysis

includes the tower base loads, platform motions, tendon tensions, tendon strength, and tendon fatigue. Also, the platform performance and tendon design are evaluated following industry standards and practices [33,34]. The modeling and simulation tool for the present work is Orcaflex [35].

## 2. Floating Wind TLP for 10 MW VAWT

### 2.1. Modular Foundation for Floating Offshore Wind Turbines

There are many key design drivers for the floating TLP's foundation (hull), which include the hull size (steel weight), tow stability, heel angle via the turbine's overturning moment, tendon pretension and ballast, tendon size and material (tendon weight), number of tendons, tendon strength and fatigue, tendon and platform installations, and mooring anchor.

If the turbine size becomes larger, the foundation dimensions to support a VAWT or HAWT also increase to balance the turbine weight and operation load (i.e., the overturning moment). A large platform can, thus, face several challenges in terms of its foundation cost, execution risk, and fabrication. For example, a conventional semi-submersible foundation with a 15 MW HAWT [4] presents about a 102 m width and 90 m length, requiring a large land space for the hull's fabrication.

A conventional TLP floating wind system (FloatVAWT) was initially designed for a lightweight platform as a baseline platform through a design optimization scheme with a project team effort during the ARPA-E ATLANTIS project [36]. Figure 2a illustrates the FloatVAWT TLP, and some results of the FloatVAWT design are presented in [16]. However, the immediate challenge we identified was how and where a large platform (e.g., 10 MW or larger) can be fabricated in a limited facility site. If a local fabrication is not available, there will be significant impacts on the cost and risk.

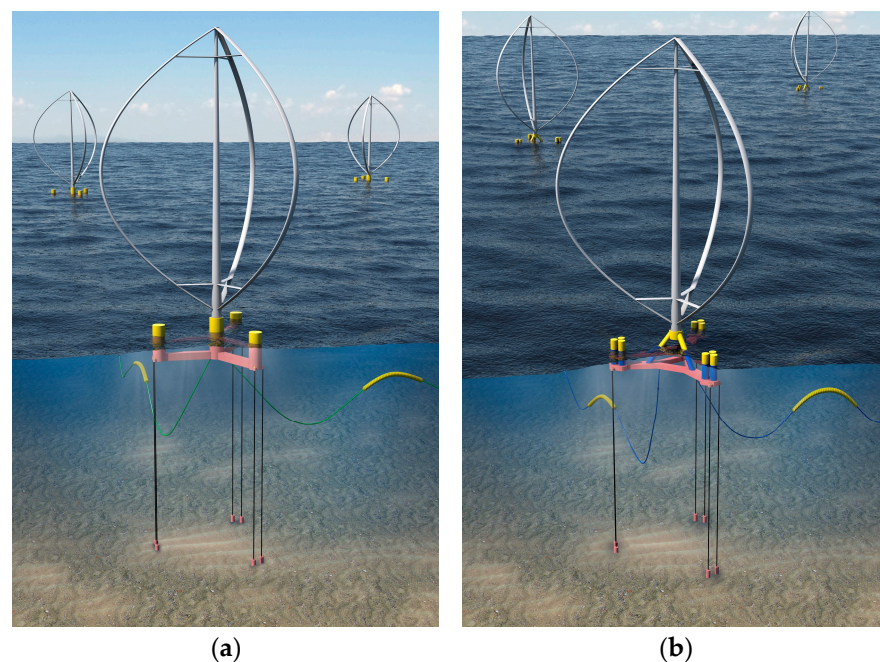


**Figure 2.** Floating wind foundations: (a) FloatVAWT TLP of conventional foundation with VAWT; (b) MarsVAWT TLP of modular foundation with VAWT.

Therefore, to achieve the ATLANTIS project's LCOE target of USD 0.075/kWh, a new concept for the foundation along with advanced turbine technology is inevitable. For this purpose, an innovative modular floating foundation is developed under the ATLANTIS project. The concept is a modular assembly and reconfigurable system (Mars) that can offer versatile applications. It is independent on the turbine (VAWT or HAWT) type or mooring (vertical or catenary) system. Figure 2b shows a TLP-type modular foundation

for a Darrieus VAWT, called “MarsVAWT”. The Mars foundation can also be used as a semi-submersible-type foundation (called “Mars-Wind”) for VAWTs or HAWTs. In the present paper, the design results of MarsVAWT for 10 MW are briefed, and the dynamic response analysis results are provided.

The MarsVAWT (or Mars-Wind) foundation consists of multiple modules of the center pontoon, outer pontoons with a node, outer columns, and a turbine support frame as depicted in Figure 3. The turbine tower is mounted at the interface node in the turbine support frame. From its outset, the platform was developed specifically to overcome US infrastructure limits on yard space, fabrication capacity, quayside draft, assembly, and integration on the West Coast, East Coast, and in Hawaii. The modular foundation allows for optimized series production that increases the fabrication efficiency and local facility utilization that expands the domestic supply while reducing the wind farm’s total cost and risk. The modular fabrication of the foundation allows for floating or onshore assembly using mechanical connections, which reduces the assembly and loadout time significantly and facilitates its assembly at more sites.

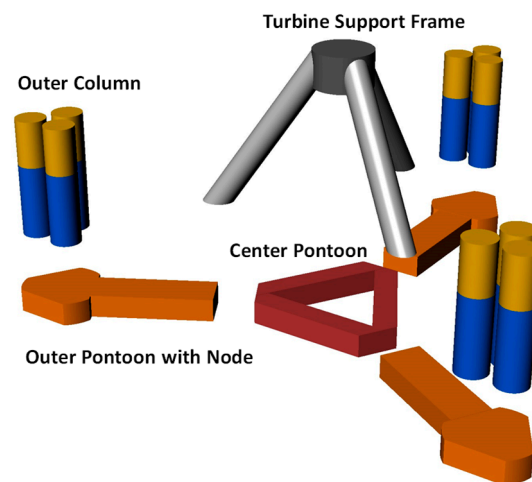


**Figure 3.** Modules of MarsVAWT (or Mars-Wind) foundation comprising center pontoon, outer pontoons with node, outer columns, and turbine support frame with turbine tower interface node.

Figure 4 illustrates a floating assembly sequence of the modules on submersible barges using mechanical connectors. The module’s assembly on water can eventually remove the platform loadout required for foundations fabricated on land. The MarsVAWT platform with a turbine integrated can be towed to the installation site to maximize execution options while reducing the execution risk. An additional feature of the modular design enables the outer columns to be reconfigurable (removable in part or full) for a TLP after the tendons are connected to reduce the hydrodynamic loads. This reconfigurable feature can eventually lower the platform mass, resulting in a low-cost foundation. In addition, it can be designed for flexible hybrid material selection for modules, e.g., steel pontoons and columns; concrete pontoons and steel columns; or steel pontoons and polymer foam (or similar) columns. The outer column can be fabricated from rolled tubulars that are within the mill capacity range. This approach can use an industrialized facility, which accelerates the column’s fabrication.

## 2.2. MarsVAWT TLP Design for 10 MW VAWT

### 2.2.1. Design of MarsVAWT

The modular TLP platform MarsVAWT is designed to support a 10 MW VAWT of the Darrieus type. The properties of the platform fabricated with steel are summarized in Table 1. The VAWT tower base with a 8.5 m diameter is integrated at the top of the interface node. It is assumed that a direct generator is installed inside the interface node. However, the details of the generators are excluded in the platform design. The lightship draft with the 10 MW VAWT integrated is about 5 m, enabling the tower to be integrated into most

ports in the U.S. The modules are sized such that the platform with the 10 MW VAWT is self-stable to allow the platform to be towable from the quayside.

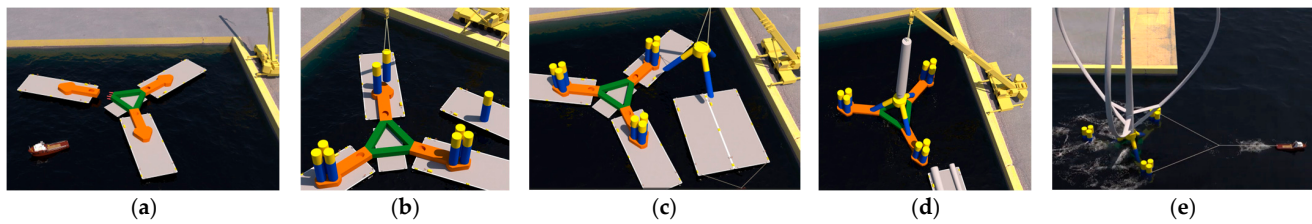


**Figure 4.** Mars-Wind module assembly sequence on quayside floating barges and platform tow to site: (a) Pontoon module assembly; (b) Outer column module assembly to the assembled pontoon; (c) Turbine support frame assembly to the assembled pontoon; (d) Foundation float-off and tower and blade integration; (e) Tow-out of the platform from quayside.

**Table 1.** Properties of MarsVAWT TLP with 10 MW VAWT.

Items	Parameter	Unit	Value
displacement and dimensions	displacement	ton	7539
	operating draft	m	16.5
	length overall	m	70.7
	outer column diameter (each)	m	5.2
	tower interface node diameter	m	10
	tower interface height above SWL	m	14
mass	turbine	ton	1858
	hull steel and water ballast	ton	2779
	vertical CoG above SWL	m	17.4

Note: “ton” and “CoG” indicate metric tons and center of gravity.

The platform is considered to be installed at a water depth of 100 m, using a vertical tendon mooring system. The top end of the tendon is connected to the keel of the outer node of the platform and the other end is connected to an anchor. The stick-up height of the anchor pile is assumed to be zero, meaning that the top of the anchor installed is located at the seabed level, which may not be a realistic installation for some anchors like a driven pile. The tendons are configured with a total of nine lines of a spiral stand wire rope. There are several other tendon material options (chain, synthetic rope, etc.). The chain was deselected through a pre-screening study due to tendon fatigue by the cyclic loadings of the VAWT. The synthetic rope was also excluded to avoid possible tendon creep and re-tensioning during the platform’s service life. According to a study of the tendon material options for a mono-column TLP wind turbine [37], a wire rope tendon demonstrates lower motion and tension than a synthetic rope. Various material options may be studied in the future to take advantage of those for very deep-water applications.

The tendon properties are shown in Table 2, including the axial stiffness (EA) and minimum breaking load (MBL). The number of lines, line size, pretension, and ballast weight have been determined iteratively using the dynamic response analysis results, complying with the tendon design requirements described in the following sections. Therefore, the ballast and tendon properties in Tables 1 and 2 are a summary of the resulting final design.

**Table 2.** Properties of tendon.

Parameter	Unit	Value
number of tendons	-	9
tendon length each	m	83.5
tendon size	mm	133
axial stiffness	kN	$1.6 \times 10^6$
MBL	kN	17,171
material type	-	spiral strand wire

2.2.2. 10 MW VAWT

The 10 MW Darrieus VAWT is a three-bladed turbine following international design standards, and its main characteristics are summarized in Table 3. Its aerodynamic pressure center is 95.4 m above the tower base. The VAWT system is optimized with intra-cycle RPM control. The turbine’s aerodynamic loads under steady winds for the VAWT were obtained using CACTUS (Code for Axial and Cross-flow TURbine Simulation) [38]. Each turbine aerodynamic load in a steady wind is normalized by its mean value at the rated wind speed of 15 m/s. The resulting load ratios are shown in Figure 5, in which the maxima, minima, and mean ratio (red marks) are presented. It is seen that the mean values of the lateral forces and torques are not zero. Therefore, the lateral forces can cause mean displacements of the platform, while the torques can create a mean yaw of the platform during the turbine’s operation. This will be investigated in numerical simulations. The turbine’s 1P, 3P, and 6P are 0.092 Hz, 0.276 Hz, and 0.552 Hz, respectively. The 3P and 6P excitations at the rated wind speed of 15 m/s are captured in the load power spectral density (PSD) plots in Figure 6.

Table 3. Properties of 10 MW VAWT of a Darrieus-type turbine.

Items	Sub-Items	Unit	Value
dimensions	rotor diameter	m	151
	swept area	m <sup>2</sup>	18,596
	number of blades	-	3
	tower height	m	187.7
	tower base diameter	m	8.5
mass	total	ton	1858
	CoG above tower base	m	42.1
operation data	cut-in/cut-out	m/s	5/25
	Rated	m/s	15
	PC above tower base	m	95.4

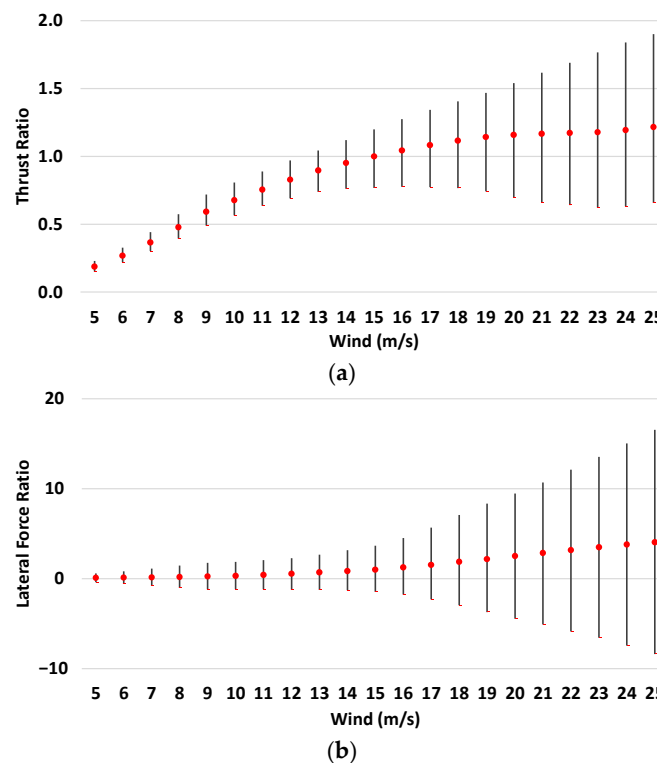
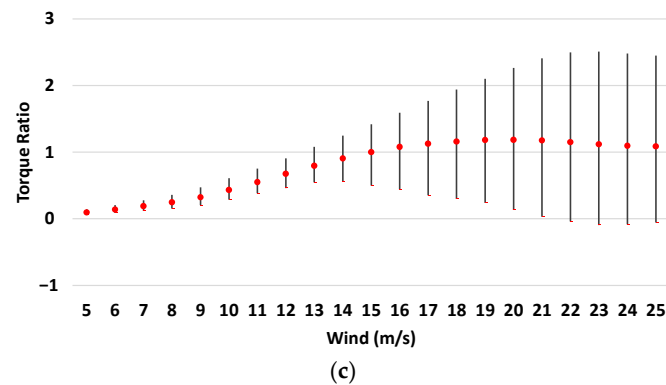
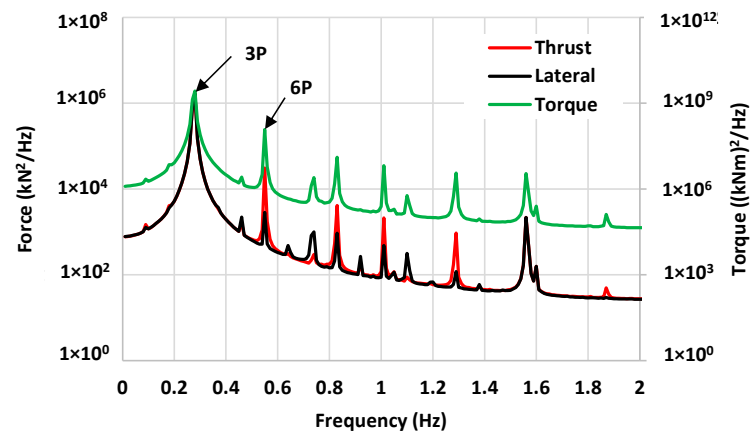


Figure 5. Cont.



**Figure 5.** 10 MW VAWT (3-bladed) turbine load ratios to the mean value at the rated wind speed (15 m/s): (a) Thrust; (b) Lateral (side-to-side) force; (c) Torque, for which the maxima, minima, and mean (red dots) ratios are presented.



**Figure 6.** Turbine load (thrust, lateral force, and torque) power spectral densities at the rated wind speed of 15 m/s.

### 3. Materials and Methods

A MarsVAWT TLP with the 10 MW VAWT system is considered for the numerical simulation to evaluate the dynamic responses and confirm the design. A coordinate system is defined in Figure 7. The reference origin is located at the platform center on the still water line (SWL). Heading definition is also provided such that the headings of 0 and 90 deg are aligned toward the positive  $x$ - and  $y$ -directions, respectively.

Tendons are numbered from T1 to T9 as depicted. Tendon tops are connected to the keel of the corresponding pontoon node and the other end is connected to the anchor. The radial anchor locations are determined depending on vertical mooring arrangement. Figure 8 depicts the tendon connection to the platform keel and anchor piles.

#### 3.1. Site and Design Load Cases

Platform installation site considered is at an offshore location in the US Northeast at a water depth of 100 m. Site metocean data are selected from the reference [39]. The resulting metocean data for the design load cases (DLCs) are summarized in Table 4.  $H_s$ ,  $T_p$ , and  $\gamma$  are the significant wave height, spectral peak period, and peak enhancement factor constructing JONSWAP spectrum. DLC 1.6 is for the VAWT turbine operating in wind from the cut-in of 5 m/s to cut-out of 25 m/s. DLC 6.1 considers a parked turbine under 50-year return period. Steady wind is used for DLC 1.6, as the turbine loads (Figure 5) are based on steady wind, while NPD (Frøya) wind model [33] is used to generate the storm winds for DLC 6.1. As site's bathymetry is unknown, a flat seabed is assumed to determine each tendon length.

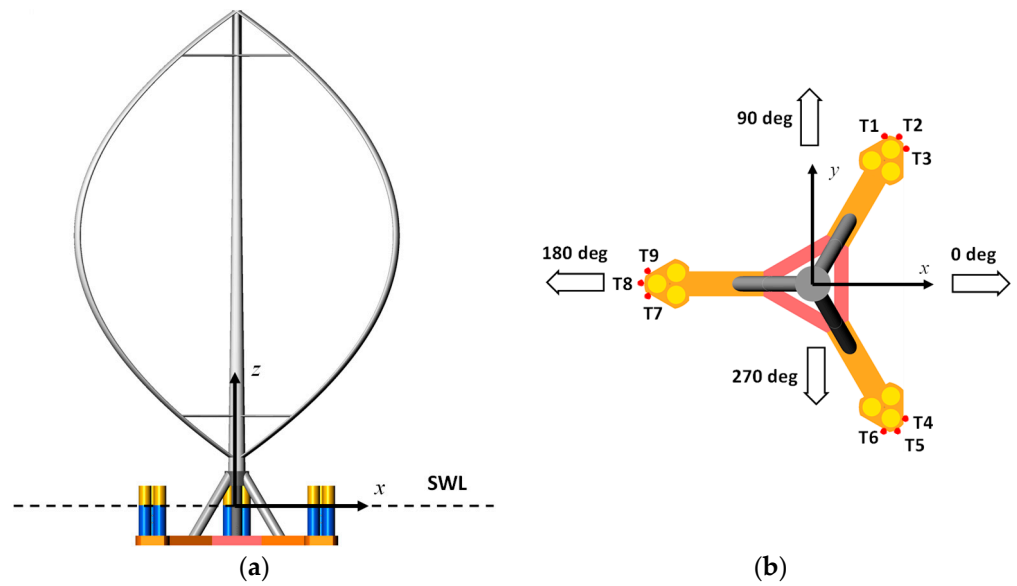


Figure 7. (a) Reference coordinate system; (b) Tendon numbering, and heading definition.

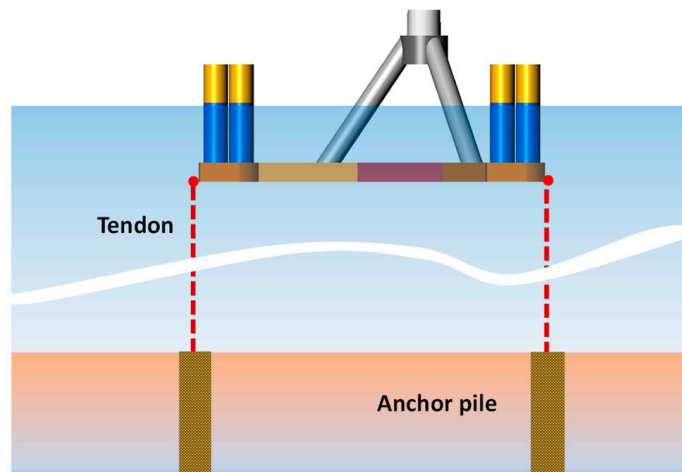


Figure 8. Tendons connected at the keel of the hull and top of the anchor pile. VAWT turbine is omitted.

Table 4. Design load cases for turbine operating DLC 1.6 and turbine parked extreme DLC 6.1.

DLCs	Wind at PC	Hs	Tp	$\gamma$	Current
	m/s	m	s	-	m/s
DLC 1.6 power production	5	6.39	11.58	2.75	0.16
	8	8.02	12.74	2.75	0.16
	10	8.1	12.79	2.75	0.16
	12	8.5	13.07	2.75	0.17
	15	9.8	13.94	2.75	0.20
	18	9.8	13.94	2.75	0.24
	20	9.8	13.94	2.75	0.27
	22	9.8	13.94	2.75	0.30
	25	9.8	13.94	2.75	0.37
DLC 6.1, parked	33.38	9.8	14.2	2.75	1.05

### 3.2. Wind and Current Drag Forces

The turbine, blades and hull exposed to air experience wind drag. The wind drag force is computed with the following equation:

$$F_{wind} = \frac{1}{2} \rho_a C_s C_h A_w V_w^2, \tag{1}$$

where  $F_{wind}$  = steady wind force,  $\rho_a$  = mass density of air,  $C_s$  = shape coefficient,  $C_h$  = height coefficient,  $A_w$  = projected area of windage on a plane normal to the direction of the considered force, and  $V_w$  = velocity of wind based on the 1-min average velocity at a reference elevation of  $z = 10$  m. The shape and height coefficients can be found in the references [33,40].

Blade pitch control is not implemented for the present 10 MW VAWT. Therefore, the wind drags increase as the wind speed increases for the parked blades. The wind drags on the parked blades are computed using CACTUS as described in the reference [15] and then implemented for the present model. Figure 9 compares the wind drags on the MarsVAWT hull, tower, and blade, as well as total wind drag including the hull, tower, and blade. Also, mean thrust forces of the turbine are plotted. Here, the turbine mean thrusts and wind drag forces are normalized by the mean thrust at 15 m/s (rated wind speed). In the platform response analysis, the total drag is used for the parked turbine (before the cut-in and after the cut-out) while the drag on the hull and tower is used for the turbine in operation.

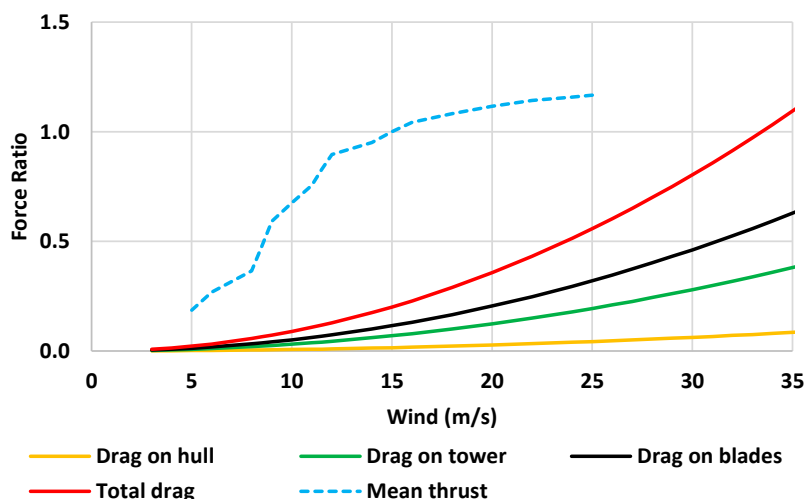


Figure 9. Wind drags on MarsVAWT with 10 MW Darrieus VAWT including hull, tower, and blades as well as total. The drag and mean thrusts are normalized by the mean thrust at the rated wind speed of 15 m/s.

The wind drag forces are imposed into the numerical model in terms of wind drag coefficients. The wind drag presented in Equation (1) is a steady force, but it becomes unsteady force in the time domain due to the relative velocities.

Due to the increasing parked drag forces, the 50-year extreme wind events may cause more significant loads than the turbine operating conditions. Also, during the turbine’s operation, the turbine loads (thrust, lateral force, and torque) continue increasing until the cut-out is reached as depicted in Figure 5. Therefore, the platform motions and tendon tensions are likely affected by the cut-out or near cut-out wind. This is a quite different phenomenon from that of horizontal axis turbines, which suggests we should consider high winds for the platform response analysis under the turbine’s operating conditions.

Current drag force on the submerged hull of the platform can be calculated using the following equation:

$$F_{current} = \frac{1}{2} \rho_w C_d A_c V_c^2, \tag{2}$$

where  $F_{current}$  = steady current force (drag),  $\rho_w$  = mass density of water,  $Cd$  = drag coefficient,  $Ac$  = projected area of the structure to the direction of the considered force, and  $Vc$  = current velocity. The projected area can vary with the current direction toward the platform. The drag coefficients can be found in the references [33,40]. The current force may be imposed using the current force coefficients as an input or implicit methods. In the present modeling, the current forces are imposed implicitly as Morison element drag. Therefore, the current force on each segment of the Morrison elements is computed considering the relative velocity between steady current and platform horizontal plane motion.

### 3.3. Platform Viscous Damping

Platform hull viscous damping is implemented in terms of Morrison drag, since the potential approach can calculate the wave damping only. The present hull has three different shapes of structures: cylinder, rectangular pontoon, and irregular-shaped node. The node is simply assumed to be a circular cylinder with the same height and volume of the original node. The Morrison elements of the outer columns and turbine support frame are extended to the top of those structures, and they are modeled with multiple segments to capture the fluid velocity variations below the instantaneous water surface. With this approach, the time varying drag forces on each segment are computed using the instantaneous wetted portion and velocity of the segment. To consider the vertical drag on the submerged structures, additional means are included for the pontoon and node. Drag coefficients used are 0.65 for the cylinder and 1.9 for the pontoon. Also, vertical drag coefficient for the pontoon and node is 4.8.

### 3.4. Time-Domain Semi-Coupled Analysis

The systems of the platform with 6-degree of freedom moored with the tendons can be solved in the time domain using the following equation:

$$(M + A(\infty))\dot{x}(t) + \int_0^t K(t - \tau)\dot{x}d\tau + (K_H + K_T)x(t) = F_{ext}(t), \quad (3)$$

$$K(t) = \int_0^\infty B(\omega)\cos(\omega t)d\omega, \quad (4)$$

where  $M$  is the mass matrix,  $A(\infty)$  is the added mass matrix at infinite frequency, and  $K_H$  and  $K_T$  are hydrostatic and tendon (mooring) stiffness matrices, respectively. The external load  $F_{ext}(t)$  includes the wind and current drag forces, wind turbine load, and wave load. The impulse response function  $K(t)$  is computed using the damping coefficients of  $B(\omega)$ . The added mass and damping force as well as wave exciting force and moment are computed with a potential-based theory in frequency domain.

In the present analysis, the equation above is solved using a semi-coupled manner in time domain. The hull and mooring are fully coupled, but the turbine loads (thrust, lateral force, and torque) are input externally at the aerodynamic pressure center of the VAWT as load time histories. This semi-coupled approach was successfully implemented in the floating TLP VAWT system analysis [16], in which whole turbine system is modeled as a rigid body and the rotation about the vertical axis (along with external turbine torque load) is considered 7th degree of freedom.

### 3.5. Flexible Tower Modeling of VAWT System

The VAWT system is split into two for modeling: flexible tower and the blade system modeled with lumped masses, called "hybrid model". The tower of the VAWT is modeled as a flexible structure presenting the same design properties, while the blade system (blades and struts) is modeled with two lumped masses. With this modeling, there are uncertainties in terms of the turbine system inertia and stiffness of the modeled turbine system. The moment of inertia as well as mass of each lumped mass and its location on the tower are,

however, tuned iteratively until the tower base loads closely converge to the loads with values from the “complete model” of the VAWT that include the tower, blades, and struts as described below.

The 10 MW VAWT loads are for a bottom-fixed turbine, which is a “complete model” in which all turbine component properties are modeled using an FEM in Offshore Wind ENergy Simulation (OWENS) toolkits [41] and correspond to the results of a dynamic analysis. For the present hybrid model validation against the OWENS results, it is also assumed the tower is mounted on the stationary rigid body of the TLP foundation to emulate the bottom-fixed turbine. As described earlier, the flexible tower and lumped blade systems are modeled using Orcaflex (version 11.3f).

The turbine loads of the thrust, lateral (side-to-side) force, and torque at the cut-out wind are imposed at the VAWT aerodynamic pressure center on the tower in time domain to simulate the tower base loads. Figure 10 compares the results of the tower base forces, bending moments, and torque for the cut-out wind, from the hybrid and complete models from OWENS. In the hybrid model, high-frequency oscillations around the peak of each cycle are observed especially in the shear forces and bending moments. Further spectral analysis shows that the high-frequency oscillations are induced by the tower with 1st and 3rd mode couplings. Tower base vertical forces ( $F_z$ ) exhibit quite different behaviors between the two models, which may be due to the modeling method of the present simplified hybrid model. But the mean value from each model is almost identical to the turbine system mass. No differences are present in the torques. Overall trends and values of the hybrid model are in good agreement with the complete model values, confirming the validity of the present hybrid model.

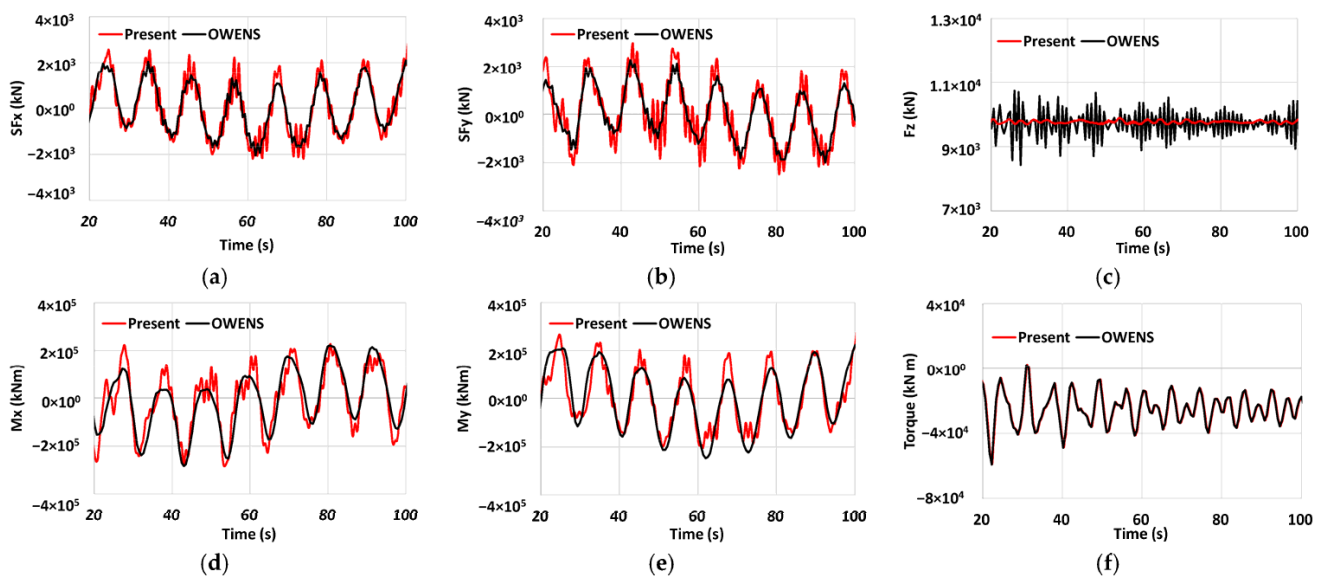


**Figure 10.** Tower base loads from the hybrid (present) and complete models (OWENS) at the cut-out wind: (a) Shear force  $SF_x$ ; (b) Shear force  $SF_y$ ; (c) Vertical force  $F_z$ ; (d) Bending moment  $M_x$ ; (e) Bending moment  $M_y$ ; (f) Torque  $M_z$ .

After the hybrid model is tuned, the turbine system eigen frequencies are computed using Orcaflex (present) and the resulting values are compared in Table 5. The frequency of the tower only from Orcaflex shows good agreement with the high-fidelity ANSYS Mechanical APDL result. It is seen that the frequency for the tower with the lumped blade mass is shifted to a lower frequency from the tower only.

**Table 5.** 10 MW VAWT Eigen frequencies.

Tower Model	1st Mode (Hz)	3rd Mode (Hz)	Analysis Tool
tower + blade lumped mass	0.209	0.816	Orcaflex
tower only	0.244	0.958	Orcaflex
tower only	0.249	0.953	ANSYS

3.6. Mooring System Stiffness

Tendon stiffness of  $K_T$  with respect to the reference coordinate system of the TLP (Figure 7) is given by the following equations:

$$K_T = \begin{bmatrix} K_{11} & 0 & 0 & 0 & K_{15} & K_{16} \\ 0 & K_{22} & 0 & K_{24} & 0 & K_{26} \\ 0 & 0 & K_{33} & K_{34} & K_{35} & 0 \\ 0 & K_{42} & K_{43} & K_{44} & 0 & 0 \\ K_{51} & 0 & K_{53} & 0 & K_{55} & 0 \\ K_{61} & K_{62} & 0 & 0 & 0 & K_{66} \end{bmatrix} \tag{5}$$

$$\begin{aligned} K_{11} &= P/L \\ K_{15} &= P/L \times (Z_{top} - Z_c) \\ K_{16} &= P/L \times (Y_{top} - Y_c) \\ K_{24} &= -P/L \times (Z_{top} - Z_c) \\ K_{26} &= P/L \times (X_{top} - X_c) \\ K_{33} &= AE/L \\ K_{34} &= AE/L \times (Y_{top} - Y_c) \\ K_{35} &= -AE/L \times (X_{top} - X_c) \\ K_{44} &= AE/L \times (Y_{top} - Y_c)^2 + P/L \times (Z_{top} - Z_c)^2 \\ K_{55} &= AE/L \times (X_{top} - X_c)^2 + P/L \times (Z_{top} - Z_c)^2 \\ K_{66} &= P/L \times [(X_{top} - X_c)^2 + P/L \times (Y_{top} - Y_c)^2, \end{aligned} \tag{6}$$

where  $K_{22} = K_{11}$ ,  $K_{42} = K_{24}$ ,  $K_{43} = K_{34}$ ,  $K_{51} = K_{15}$ ,  $K_{53} = K_{35}$ ,  $K_{61} = K_{16}$ , and  $K_{62} = K_{26}$ . Also,  $P$  = tendon pretension,  $L$  = tendon length,  $AE$  = tendon axial stiffness,  $(X_{top}, Y_{top}, Z_{top})$  = tendon top coordinates, and  $(X_c, Y_c, Z_c)$  = reference coordinates with respect to SWL.

Table 6 compares the tendon stiffness values from the numerical simulation with the theory in Equation (6). The difference presented is the relative ratio to the theory. The numerical tendon stiffnesses are in good agreement with the theory, validating the tendon modeling.

**Table 6.** Tendon stiffness from the numerical simulation and theory.

Method	$K_{11}$ kN/m	$K_{15}$ kN/rad	$K_{24}$ kN/rad	$K_{33}$ kN/m	$K_{44}$ kNm/rad	$K_{55}$ kNm/rad	$K_{66}$ kNm/rad
Simulation	333	-5495	5495	172,347	$1.87 \times 10^8$	$1.87 \times 10^8$	$7.24 \times 10^5$
Theory	341	-5625	5625	172,347	$1.87 \times 10^8$	$1.87 \times 10^8$	$7.41 \times 10^5$
Difference (%)	-2.32	-2.32	-2.32	0.00	-0.04	-0.04	-2.32

3.7. Platform System Identification

3.7.1. Offset, Setdown, and Restoring Force

For the TLP, when the platform is displaced from the static equilibrium position (called offset), then the platform is vertically pulled down from the SWL (called setdown) with an

angle of rotation due to the tendon force. The setdown  $Z_{setdown}$  can be also approximated assuming no platform rotation occurs at an offset as follows:

$$Z_{setdown} = -L \left[ 1 - \sqrt{1 - (X_{offset}/L)^2} \right] \quad (7)$$

where  $L$  and  $X_{offset}$  are the tendon lengths before elongated and platform offset, respectively.

Figure 11a shows the surge restoring force and surge stiffness due to the offset in the  $x$ -direction, where the restoring force and offset are normalized by the pretension and water depth, respectively. The surge stiffness curve (slope of the restoring force curve) illustrates the nonlinear behavior of the surge stiffness (or restoring force). The surge stiffness is also compared with the linear stiffness  $K_{11}$  (333 kN/m, marked value) in Table 6. An excellent agreement between the two is presented, validating the surge stiffness from the slope at small offset around the initial static equilibrium position (zero offset).

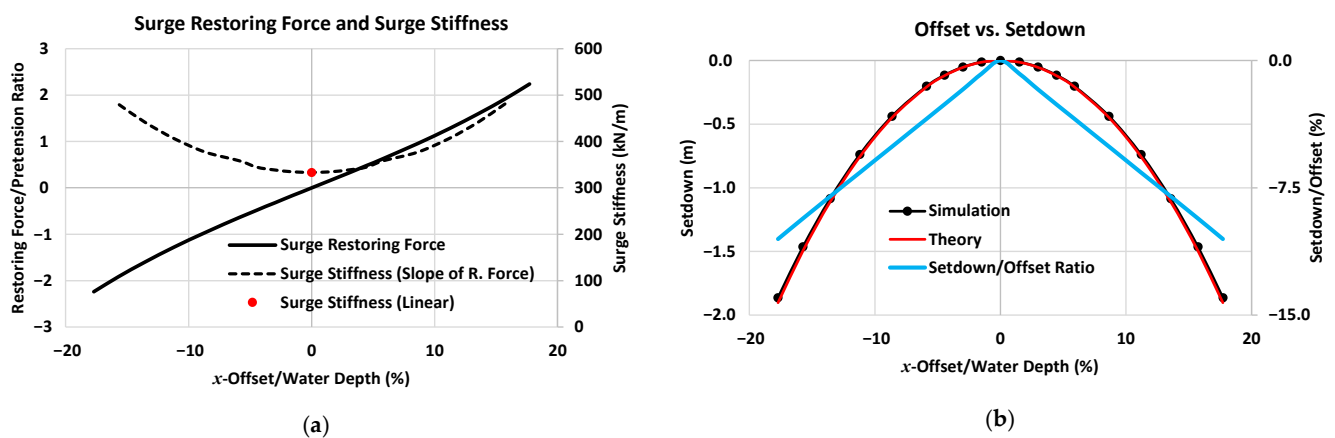


**Figure 11.** Platform offset, stiffness, and setdown: (a) Surge restoring force and surge stiffness due to offset; (b) Offset vs. setdown.

Figure 11b plots the offset vs. setdown curves of the MarsVAWT 10 MW TLP from the simulation and theory. For the numerical offset tests, incremental forces are applied in the  $+x$  and  $-x$  directions at the platform coordinate reference center but allow for the platform rotations. The simulation results are in good agreement with the theoretical approximations. It is also seen that the setdown ratio to the offset varies linearly. At an offset of  $\pm 10$  m (10% of the water depth), the setdown is about 6% of the offset. With this result, we can roughly estimate a static setdown at a high static offset. In the TLP design point of view, the setdown is an indication of airgap reduction of the platform. The present design of the MarsVAWT maintains a sufficient airgap to the tower base.

Displaced volume of the platform is augmented by the volume induced by the setdown, resulting in the tendon tension increase by the increased buoyancy. Among the tendon groups, the middle tendons of T2, T5, and T8 are selected, and their offset vs. tensions are compared for the  $x$ - and  $y$ -directional offset cases in Figure 12. Here, the tension and offset are normalized by the tendon pretension and water depth, respectively. Non-linear variations in the tensions due to the offsets are shown.

### 3.7.2. Platform Decay Tests and Natural Periods

Decay time histories for the surge, heave, pitch, and yaw are plotted in Figure 13, in which the flexible and rigid tower cases are compared. The rigid tower is modeled simply by replacing the tower bending stiffness with a sufficiently large value. The decays for the surge, heave, and yaw are nearly the same between two tower models, whereas the pitch decays (roll not shown here) are different between the two. The pitch decay of the platform with the flexible tower shows some irregularities in the decay pattern and duration between the peaks, likely due to the tower flexibility. For a further validation

of the present tower model, additional model of a rigid body is considered such that the platform hull and VAWT system are modeled as a single rigid body, like the approach of [16]. Pitch decay of the rigid body is compared in Figure 13c. Other motion decays are excluded in this comparison since there is no noticeable difference from the flexible or rigid tower model results. As seen, the pitch decay of the rigid tower is almost identical to the rigid body result, meaning that the rigid tower model emulates the rigid body model. As observed from the comparison simulations, it is confirmed that the flexible tower is coupled to the platform pitch, resulting in irregular decay. Platform’s natural periods (and frequencies) derived from the decay tests are given in Table 7. Roll and pitch natural periods of the platform with the flexible tower are shortened compared to those of the rigid tower. Because of the irregularity of the decay time histories for the flexible tower, the natural frequencies of the roll and pitch are determined using a spectral analysis. Constant damping is calculated using the logarithmic decrement at the 7th cycle from the decay time histories. The resulting damping coefficients are 3.21% for the surge, 2.55% for the heave, 2.7% for the pitch, and 1.04% for the yaw. The damping coefficients need to be correlated with experimental results when available.

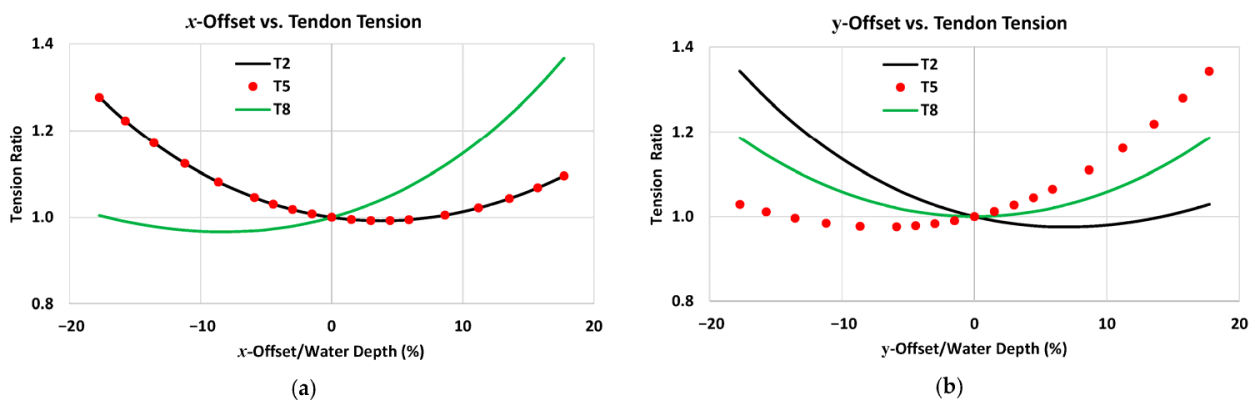


Figure 12. Tendon tension due to the platform offset: (a) Platform offset in *x*-direction vs. tendon tension; (b) Platform offset in *y*-direction vs. tendon tensions.

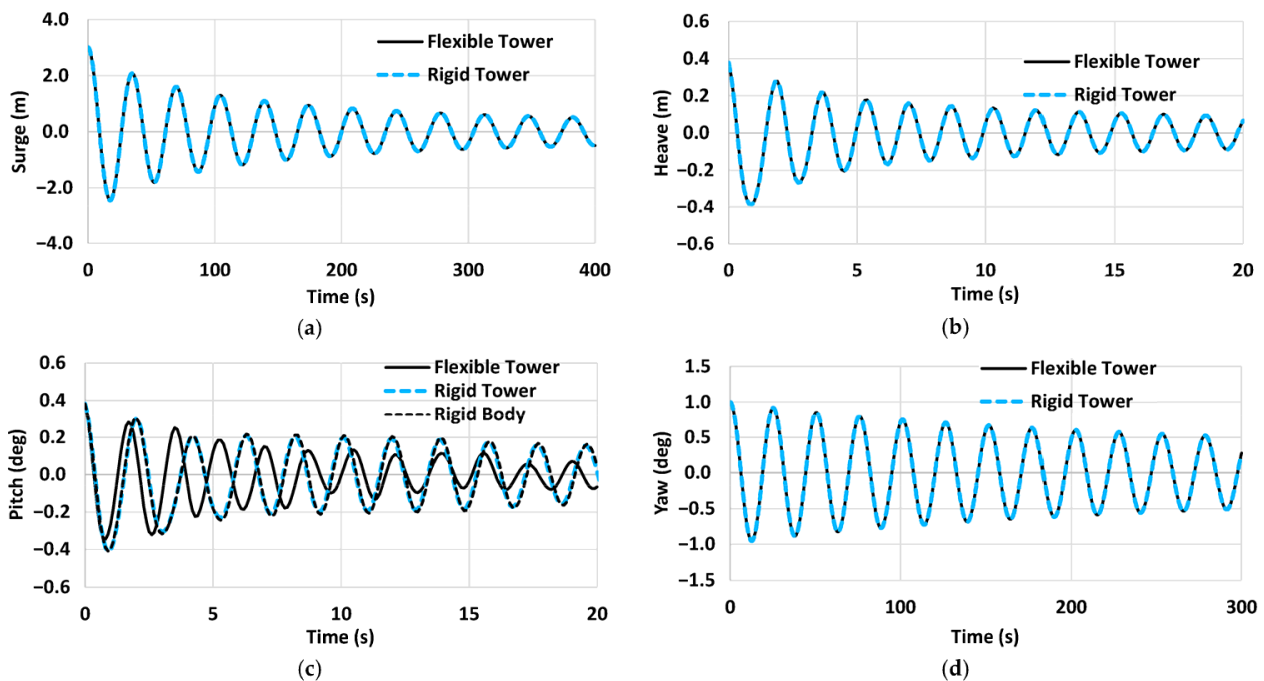
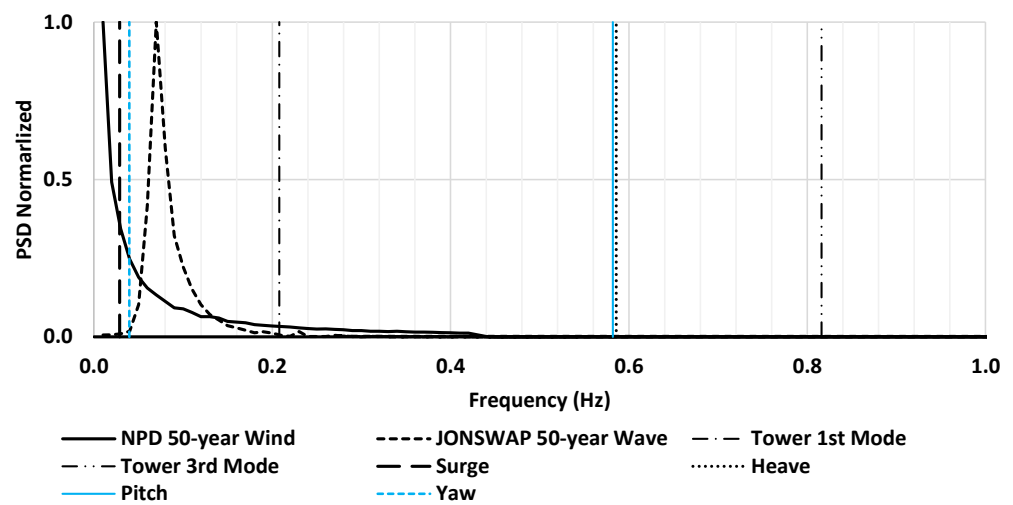


Figure 13. Decay time histories of the platform with the flexible tower and rigid tower: (a) Surge; (b) Heave; (c) Pitch; (d) Yaw.

**Table 7.** Platform’s motion natural periods (or frequencies).

Tower Model	Surge	Sway	Heave	Roll	Pitch	Yaw
flexible tower, s (Hz)	34.76 (0.03)	34.76 (0.03)	1.71 (0.59)	1.72 (0.58)	1.73 (0.58)	25.17 (0.04)
rigid tower, s (Hz)	34.76 (0.03)	34.76 (0.03)	1.71 (0.59)	1.92 (0.53)	1.93 (0.52)	25.17 (0.04)

Figure 14 compares the platform’s natural frequencies of heave, pitch, and yaw, as well as 1st and 3rd modes of the 10 MW VAWT tower. Here, the wave and wind PSDs are normalized with its own maximum. It is seen that the platform’s natural frequencies of the heave and pitch (and roll) are far off the wave excitation frequency, which is a TLP design practice. Also, the tower’s natural frequencies are sufficiently separate from the heave and pitch resonances. Natural frequency of the platform pitch with flexible tower (0.58 Hz) is higher than the frequency (0.52 Hz) of the platform with the rigid tower. This is an opposite result to that of a study of a mono-column TLP with a HAWT [42].



**Figure 14.** Platform and tower natural frequencies, and wind and wave PSD normalized with maximum value.

### 3.7.3. Platform and Tower Base Load RAOs

Response amplitude operators (RAOs) are computed with three different methods: time-domain white noise (WN) waves, frequency-domain method (FD), and regular waves. The white noise waves use a significant wave height ( $H_s$ ) of 4 m and present a spectral density of about  $1 \text{ m}^2/\text{Hz}$ . The same  $H_s$  of 4 m is also used for the frequency domain analysis. The regular waves used have wave height of 2 m with wave periods between 2 s and 50 s. For the short periods of the regular waves, the wave heights are adjusted to avoid breaking waves. Figure 15 presents the platform RAOs of the surge, heave, pitch, and T8 tension for a wave heading of 0 deg. The tendon selected is the weatherside tendon T8. All three methods capture the platform’s natural frequencies obtained from the decay tests. The three model results are shown to be in good agreement in the frequency range below about 0.5 Hz, except for the heave. High coupling effects due to the tower (1st mode, 0.21 Hz) are presented in the pitch and tension RAOs. The tower’s effect in the pitch RAOs can be anticipated from the pitch decay test described earlier. Also, the tower’s 3rd mode effect (0.82 Hz) is also observed in the pitch and tension RAOs.

Figure 16 compares the tower base load RAOs of the shear force in the  $x$ -direction  $SF_x$  and bending moment  $M_y$  about  $y$ -axis. Component frequencies from the wave and pitch, as well as the 1st and 3rd modes of the tower are seen. Among them, the tower’s 1st mode effect is the most prominent.

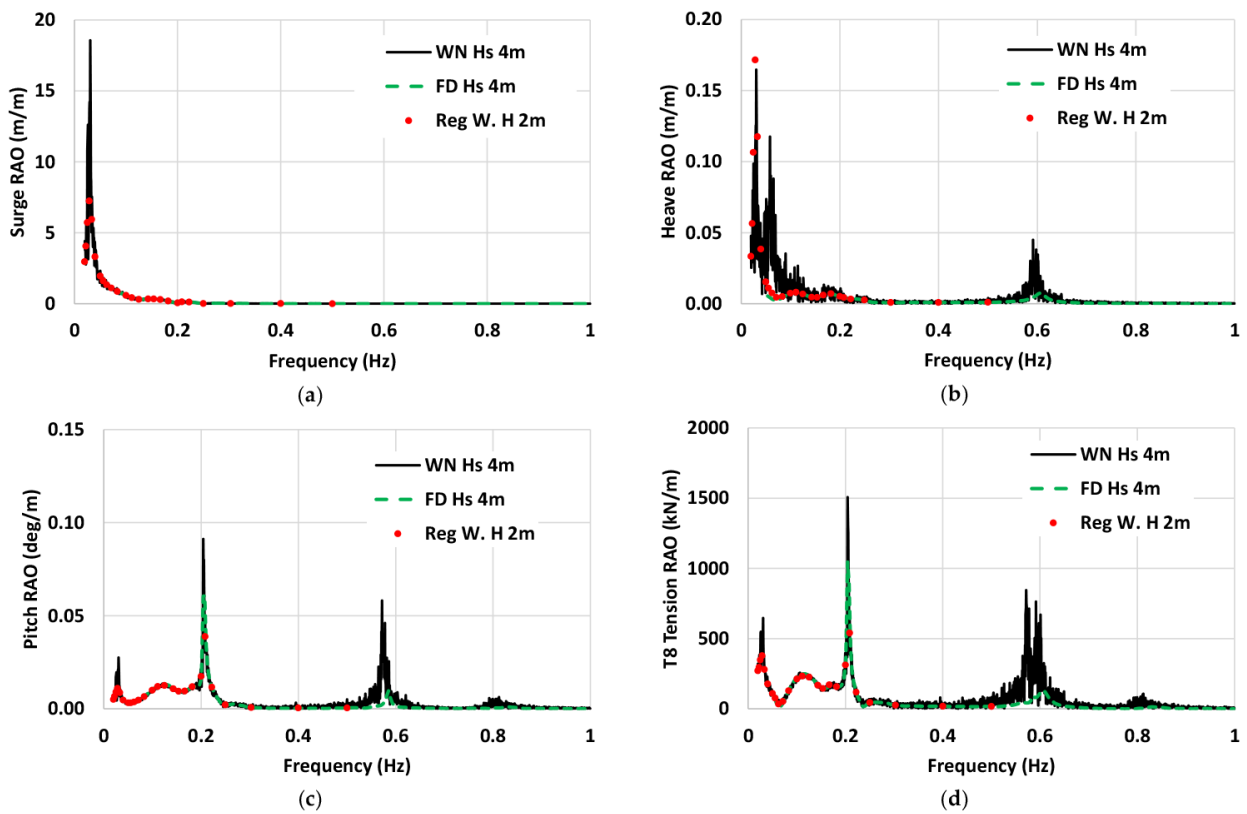


Figure 15. Platform and tendon tension RAOs: (a) Surge; (b) Heave; (c) Pitch; (d) Tendon tension T8.

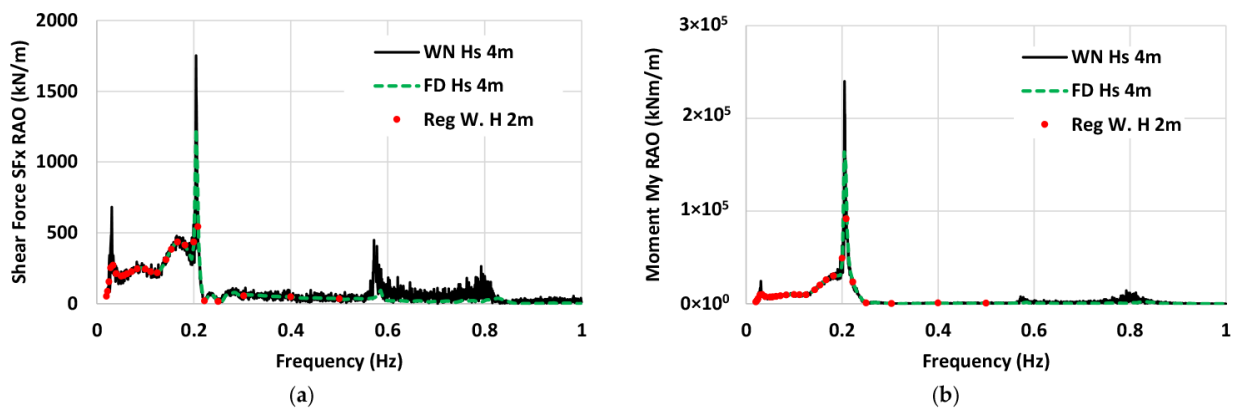
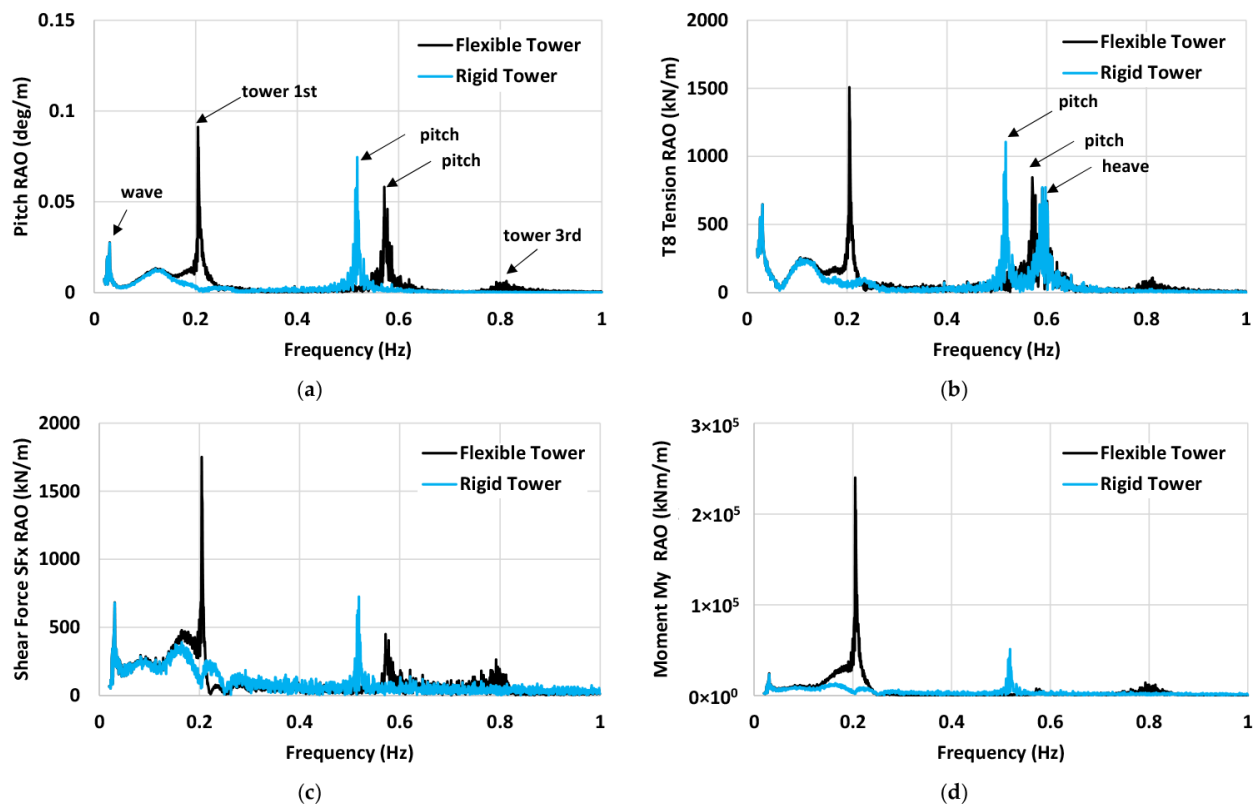


Figure 16. Tower base load RAOs: (a) Shear force SFx; (b) Bending moment My.

RAOs of the platform with the flex tower and rigid tower are also compared in Figure 17. The tower eigen mode frequencies are not present in the rigid tower model as anticipated. But the platform pitch resonance is shifted from the frequency (0.58 Hz) for the flexible tower to a lower frequency of 0.52 Hz for the rigid tower, as also presented in Table 7. The result shows a different trend of the frequency shift presented in [43], in which a mono-column TLP with a HAWT was used. Further study may be needed to find cause of the difference. The T8 tension RAOs of the flexible tower show the platform pitch component only, while the rigid tower presents the coupled effects due to both platform's heave and pitch. RAOs of the shear force and bending moment for the flexible and rigid towers present nearly the same trend to that of the pitch RAOs in terms of each component's peak location.



**Figure 17.** RAO comparisons between flexible and rigid towers: (a) Platform pitch; (b) T8 Tension; (c) Tower base shear force  $SF_x$ ; (d) Tower base moment  $M_y$ .

#### 4. Results and Discussion

Simulations are performed for the MarsVAWT platform with the flexible 10 MW VAWT under the conditions of DLC 1.6 and DLC 6.1. The platform and mooring properties are provided in Tables 1 and 2. The duration of each simulation is one hour for DLC 1.6 and three hours for DLC 6.1, excluding the initial ramp-up and transient state. As mentioned earlier, a steady inflow wind is used for the operating conditions of DLC 1.6 while the NPD wind spectrum is used for the parked turbine conditions of DLC 6.1. The DLC 6.1 simulations include all the environmental components of the wind, waves, and current.

For the DLC 1.6 simulations, we consider two different sets. The first set is to evaluate the individual load effect due to the turbine and waves. In the first set, the three loading cases considered are as follows: the wind only, the waves only, and the combination of the wind and waves. The wind-only condition is simulated without the waves so that the responses induced by the pure turbine loads of the thrust, lateral forces, and torques can be investigated. Similarly, the wave only uses the waves without considering the turbine loads, while the wind–wave combination considers both the wind and waves. The wind drags on the hull and turbine, and the current drags are excluded for these simulations. The wind and wave headings considered are 0 deg. The first set of results are presented Sections 4.1–4.4. The second set considers the environment of the wind, waves, and current. The second set of results are described in Section 4.6. Again, a co-directional environment heading of 0 deg is considered.

##### 4.1. Turbine Responses with Flexible Tower (DLC 1.6)

The tower's base shear forces ( $SF_x$ ,  $SF_y$ ), bending moments ( $M_x$ ,  $M_y$ ), and torque ( $M_z$ ) are considered for both cases: the wind only and the combination of the wind and waves. The shear forces and moments are normalized by the mean of the shear force  $SF_x$  and the mean of the moment  $M_y$ , respectively. The mean value used for the normalization

is extracted from the mean value at the rated wind speed of 15 m/s for the wind–waves combination. As described, the codirectional heading of the wind and waves is 0 deg.

The resulting ratios of the maximum and mean of the shear forces, bending moments, and torque at the tower base are compared in Figures 18 and 19. Here, the normalized maximum and mean are presented with bar and line charts, respectively. The dynamic values are not presented in these plots, but they can be estimated by the “maximum minus mean”, which is the magnitude above the mean value line.

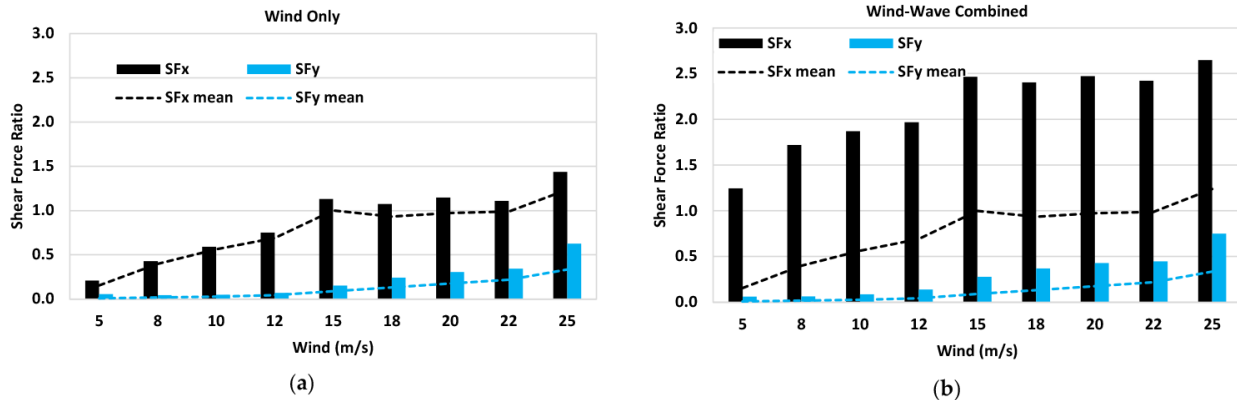


**Figure 18.** Ratio of the maximum and mean of the shear force at the tower base: (a) Wind only; (b) Wind–waves combined. The ratio is the normalized maximum or mean by the mean at the rated wind speed for the wind–waves combination.

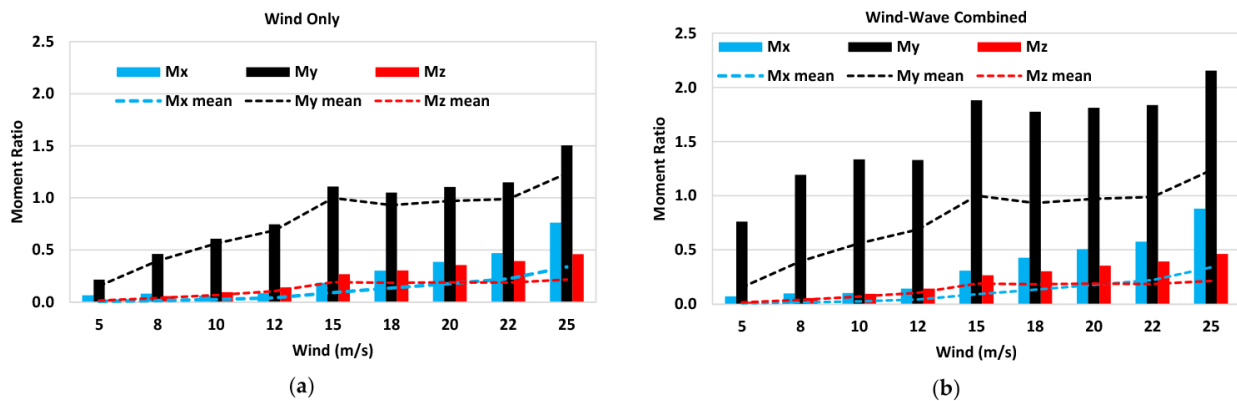


**Figure 19.** Ratio of the maximum and mean of bending moments and torque at tower base: (a) Wind only; (b) Wind–waves combination. The ratio is the normalized maximum or mean via the mean at the rated wind speed for the wind–waves combination.

Figure 18 shows the gradual increase in the mean shear forces of  $SF_x$  as the wind speed increases. The mean ratios of the  $SF_x$  for the wind–waves combination are nearly the same as those for the wind only. However, there are large increases in the dynamic  $SF_x$  for the wind–waves combination due to the coupling effects that are mostly due to the platform’s motions in waves. The dynamic shear forces ( $SF_x$ ,  $SF_y$ ) for the wind only are small, although there are large oscillating dynamic loads around the mean as seen in Figure 5. The shear forces of  $SF_y$  are much smaller than those of  $SF_x$ , indicating the thrusts cause higher tower base loads than the lateral forces.

Figure 19 plots the ratio of the moment  $M_x$ ,  $M_y$ , and  $M_z$  (torque). The computed  $M_x$  and its mean values are negative, but for the comparison, the absolute values are plotted. The bending moment  $M_y$  for the wind only is much greater than the  $M_x$ . The mean values of the  $M_y$  between the wind only and the wind–waves combination are nearly the same. Like the shear force, the dynamic variations of the  $M_y$  are small for the wind only but large for the wind–waves combination. The largest tower base bending moments ( $M_x$ ,  $M_y$ ) occur at the cut-out wind with the wind–waves combination.

The results of the tower base shear force  $SF_x$  and bending moment  $My$  suggest that the tower design should consider the effects of the platform's motion on waves.

4.2. Platform Motion Responses (DLC 1.6)

The platform's motion responses due to the three different load cases are presented in Figure 20, in which the dynamic motions (bar graphs) and their mean values (lines) are shown.

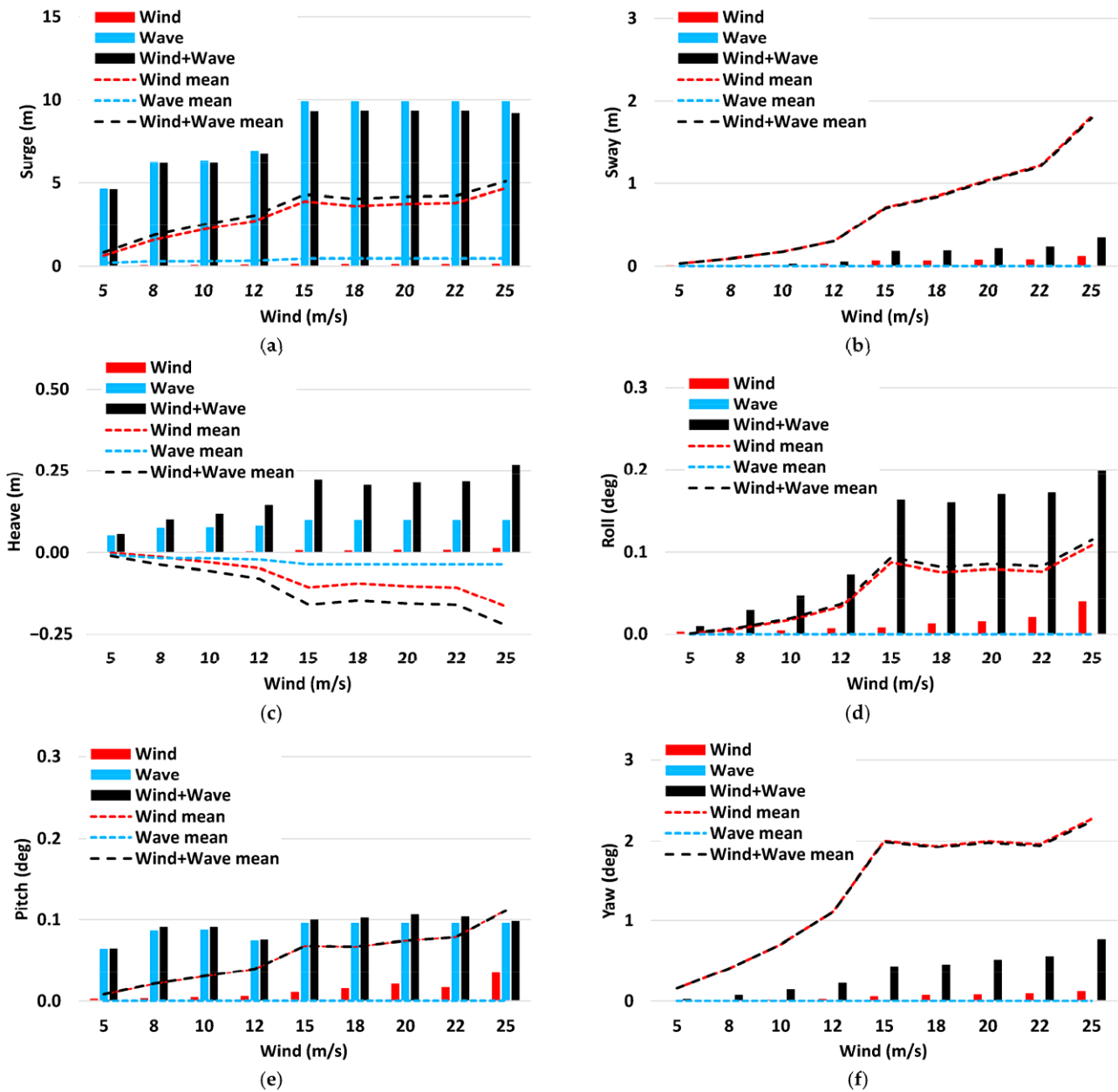


Figure 20. Dynamic and mean of platform motions for DLC 1.6: (a) Surge; (b) Sway; (c) Heave; (d) Roll; (e) Pitch; (f) Yaw.

The mean surges of the wind only and the combination of the wind–waves (“Wind + Wave”) gradually increase until the rated wind speed of 15 m/s, and then they stay the same with some small changes. The surges by the wind only are very small, compared to those by the waves only. The total surge displacement (mean + surge) by the wind only (wind 15 m/s to 25 m/s) is about 14% of the water depth. The dynamic sway is observed to be very small for all three cases. The turbine loads cause a higher setback (negative

mean heave) of the platform than that of the waves. Heaves by the wind only are, however, much smaller than those of the waves.

The roll and pitch mean values are similar, but rolls of the combination of the wind–waves beyond the rated wind speed are greater than the pitch. The maximum angle (mean + dynamic) is about 0.3 deg for the roll and 0.2 deg for the pitch during the turbine’s operation. The yaw responses show different characteristics from the roll and pitch. The total effective stiffnesses for the roll and pitch are generated by the platform’s hull geometry, mass center, and tendons, but the yaw stiffness is from the tendons only. Therefore, there are large mean yaws induced by the VAWT’s mean torque, which is much greater than the roll or pitch mean. This result indicates that a quite high mean yaw of the platform may occur for a TLP with a longer tendon at a deeper water depth than 100 m considered in the present analysis. Overall, the cut-out wind (wind only and the combination of the wind–waves) creates the greatest motion responses.

Figure 21 compares the platform in-plane motion trajectories at a wind speed of 25 m/s. The platform experiences a very small dynamic horizontal displacement for the wind only (Figure 20a), while the waves dominate the motion causing highly dynamic surge displacements as presented in Figure 20b.

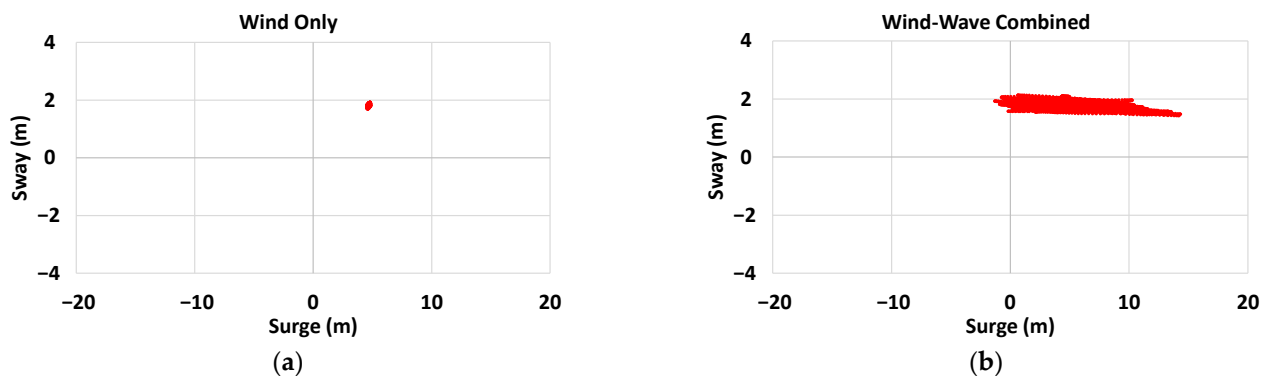


**Figure 21.** Platform motion trajectories at a wind speed of 25 m/s: (a) Wind only; (b) The combination of wind–waves.

#### 4.3. Tendon Tension Responses (DLC 1.6)

The middle tendons of T2, T5, and T8 among each tendon group are selected. Figure 22 shows the dynamic tension ratios at the top of the tendons induced by the wind only, waves only, and the combination of the wind–waves. The tension ratio is the dynamic tension normalized by the T8 dynamic tension at the rated wind speed (15 m/s) for the combination of the wind–waves. The dynamic tension is the maximum tension subtracted by the pretension. The tendon T8 is in the weatherside so that it experiences a higher tension than that of the leeside tendons of T2 and T5. The T5 tension by the wind only is reduced from the pretension due to the sway and rotational motions. The tensions by the waves only are much greater than the tension by the wind only. Also the effects of the combination of the wind–waves are more noticeable in the weatherside tendon of T8. The T8 tension ratio for the combination of the wind–waves exceeds 1.0 at the cut-out wind, showing that the tendon strength design for the operating condition is likely governed by the cut-out or near cut-out wind.

The wind-only case is again considered further to identify the most dominant turbine load component in the tendon tension increase. Simulations are run for the thrust only, the lateral force only, and the torque only, and then the dynamic tendon tensions on the tendons T2, T5, and T8 are normalized by the T8 tension induced by the thrust only. The resulting dynamic tension ratios are compared in Figure 23. Among the turbine load components, the turbine thrust is the most dominant component affecting the tendon tension increase. The torque’s contribution to the dynamic tension increase is exceedingly small.

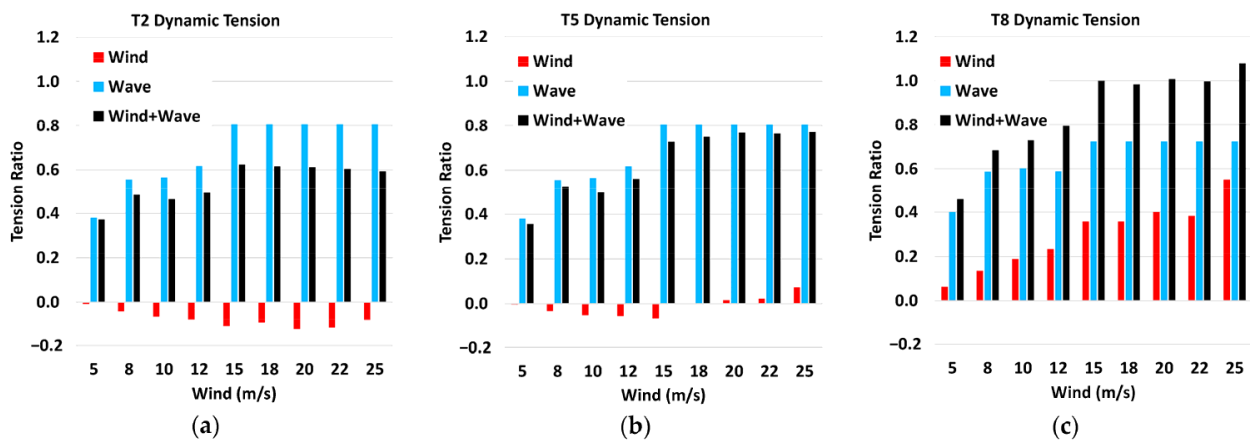


Figure 22. Tendon dynamic tension ratios for the three different cases of the wind only, waves only and the combination of the wind–waves for DLC 1.6: (a) T2 tension; (b) T5 tension; (c) T8 tension. The tension ratio is the tension normalized by the T8 dynamic tension at the rated wind speed for the combination of the wind–waves.

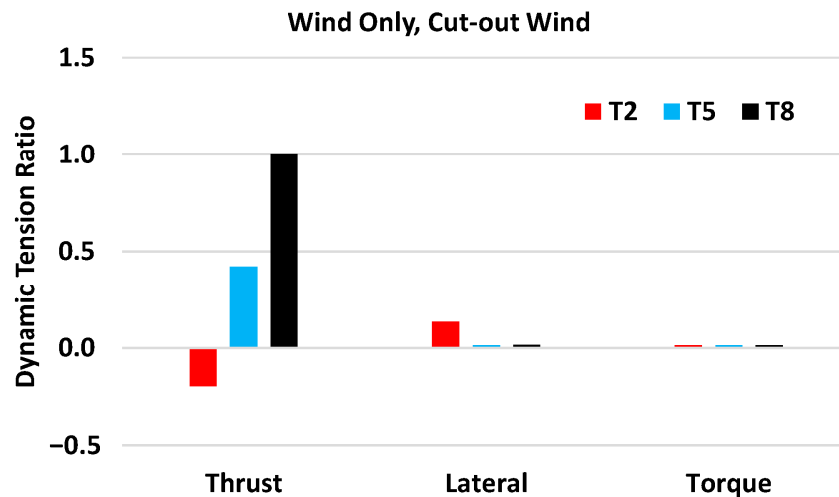


Figure 23. Dynamic tendon tensions due to the individual thrust, lateral force, and torque at the cut-out wind speed of (25 m/s). The tension ratio is the tension normalized by the T8 tension induced by the thrust at the cut-out wind speed.

4.4. Power Spectral Densities (DLC 1.6)

Figure 24 shows the PSD of the tower base shear force  $SF_x$ , bending moment  $M_y$ , platform pitch, and T8 tension at the rated wind speed. The coupling effects of the tower’s 1st and 3rd modes as well as turbine’s 3P and 6P are presented for all the responses as shown in these plots. But the 3P on the shear force is small for the wind-only case and almost disappears for the combination of the wind–waves, since the waves may have more dominant effects on the shear force than the turbine at that frequency. The 6P and pitch have almost the same resonant frequencies so they are barely differentiable on the PSD plots.

4.5. Tendon Tensions for DLC 6.1

DLC 6.1 is analyzed for the environment headings 0 to 180 deg with an increment of 15 deg, excluding some angles due to symmetry. Three-hour simulations are run for each heading assuming co-directional winds, waves, and currents. The NPD wind spectrum is considered. The parked wind drag force (Figure 9) is applied in the simulation at the pressure center of the VAWT. As mentioned earlier, in the simulation, the wind drags are calculated using the relative velocities between the undisturbed wind and platform motions.

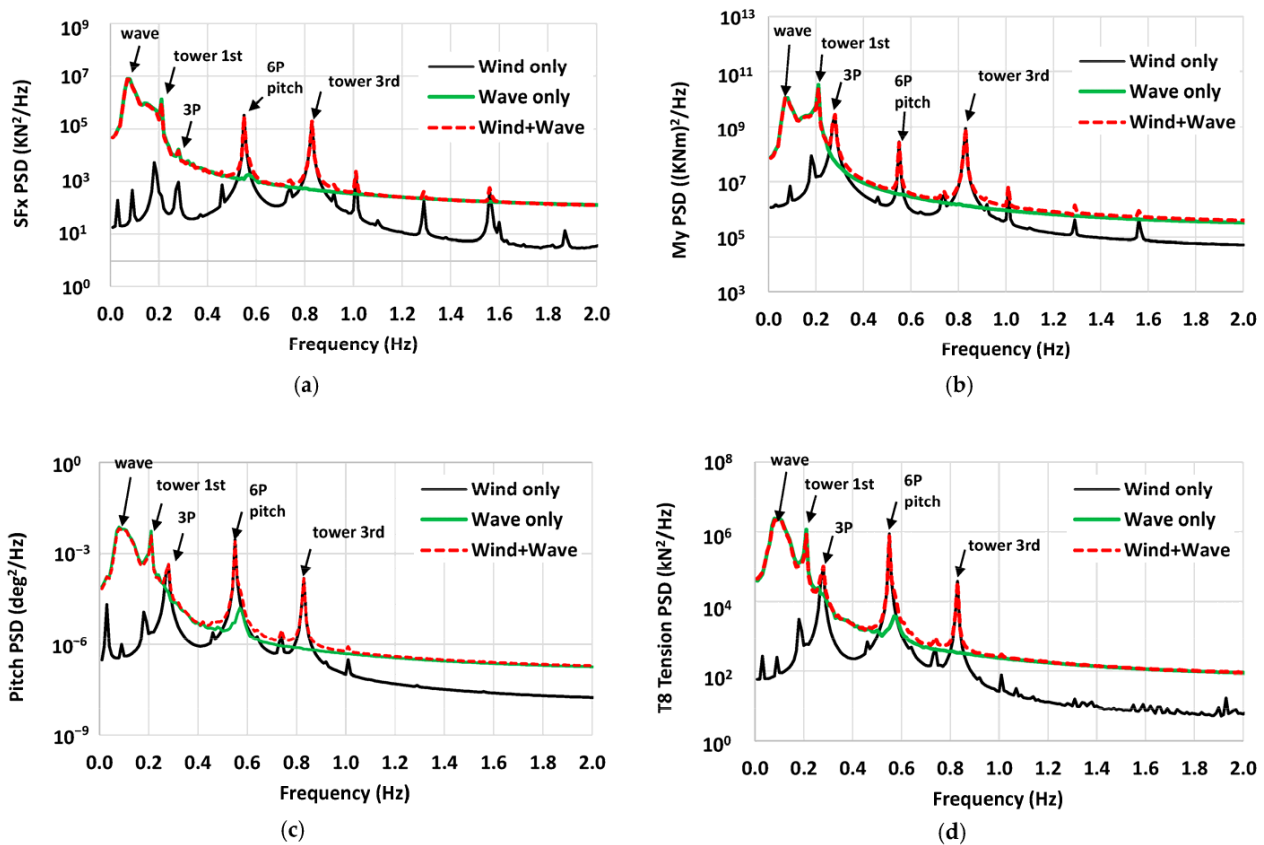


**Figure 24.** PSD of tower base load, motion, and tension at the rated wind speed of 15 m/s for DLC 1.6: (a) Shear force  $SF_x$ ; (b) Bending moment  $M_y$ ; (c) Platform pitch; (d) T8 tension.

The extreme values for the responses can be calculated using a statistical method. For example, the extreme tension may be calculated using the following equation [44]:

$$T_{extreme} = T_{mean} + 2\sigma_T \times \left[ -0.5\ln\left(1 - p^{1/N}\right) \right]^{1/2}, \tag{8}$$

where  $T_{extreme}$ ,  $T_{mean}$ ,  $\sigma_T$ , and  $p$  are the extreme tension, mean tension, standard deviation of the tension, and probability, respectively.  $N$  is the number of cycles from the 3-h time domain simulation. The tension at the 90% percentile ( $p_{90}$ ) level is taken as an extreme value for the present analysis. The tendon strength performance is evaluated using the factor of safety (FoS) as follows:

$$FoS = T_{extreme} / MBL, \tag{9}$$

where  $MBL$  is the tendon’s minimum breaking load. The dynamic amplification factor (DAF) of the tension can be given as follows:

$$DAF = T_{extreme} / P, \tag{10}$$

where  $P$  is the tendon pretension.

Figure 25 shows the extreme tension ratio, FoS, and DAF of the tendons of T2, T5, and T8, for which the tensions at the tendons’ tops are considered. The tension ratio is defined as the tension normalized by the largest tension. The adjacent tendons to the middle tendon show the almost same tensions as those of the middle tendon in the same group, so they are omitted. The extreme tensions vary with the heading angles. The largest tension occurs at the heading of 90 deg (or 30 deg). Weatherside tendons (e.g., T8 for 0 deg, T5 for 90 deg) experience higher tension, compared to leeside tendons. The same results are also found in

DLC 1.6, for which a heading of 0 deg is considered. Figure 25b shows the FoS values of the tendons. They are greater than the required minimum of 1.67 for the intact and redundant mooring system [33].

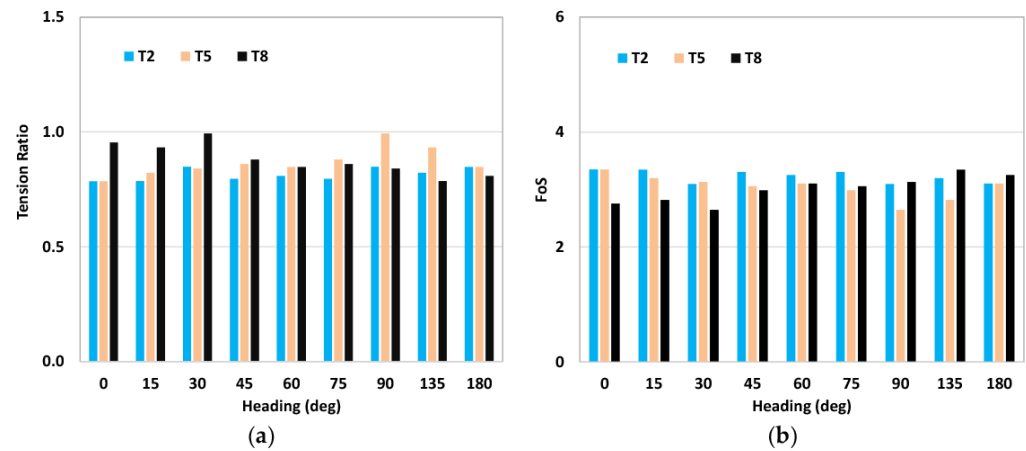


Figure 25. Tendon top tensions for DLC 6.1: (a) Extreme tension ratio of tendons T2, T5, and T8 to the maximum tension; (b) FoS of tendon.

The maximum and minimum DAFs of tension in Figure 26 are about 2.0 and 1.5, respectively, indicating that the extreme tensions are increased by roughly 1.5 to 2 times more than the pretension for the 50-year extreme conditions.

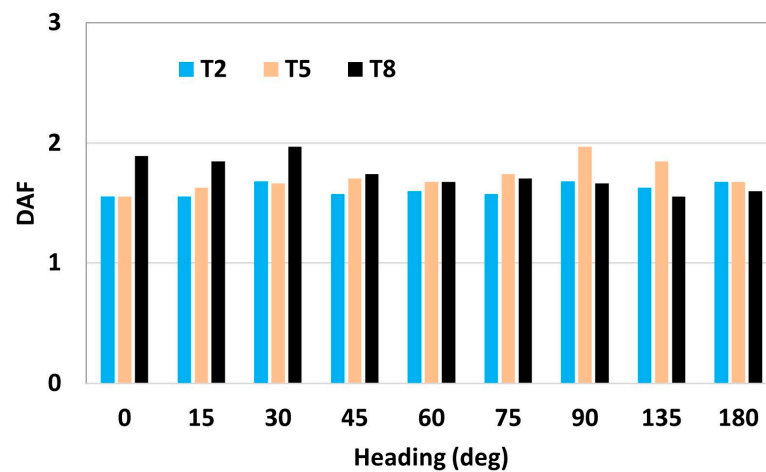


Figure 26. Dynamic amplification factors of tendon tension for DLC 6.1.

The TLP’s design requires that the minimum tendon tension at the anchor is positive to prevent tendon slack which might cause snatch loads. According to the ABS [33], the tendon slack may be acceptable if the snatch loads are considered in the design. For this, the minimum tendon tensions at the anchor are further evaluated, and the normalized anchor tensions by the pretension are compared in Figure 27. It shows that the tendons remain in tension, confirming the tendons’ design compliance. The magnitude of the minimum tension is, however, about 5% of the pretension for certain tendons and headings. Further simulations are, therefore, suggested using multiple realizations to confirm the minimum tension as positive.

#### 4.6. Extreme Motion and Tension Ratio Relative to DLC 1.6

In this section, we consider DLC 1.6 again, but this this time, it considers all the environments of the wind, waves, and current. A co-directional heading of 0 deg and steady inflow wind are considered for DLC 1.6. The wind drag force on the tower and hull and the current force are also included. Among the wind speeds of DLC 1.6, the winds

from the rated to the cut-out wind speed are selected. The extreme responses for DLC 6.1 for the heading of 0 deg are extracted from the results described in Section 4.5. For the comparisons below, the response ratio is used, which is calculated as the response of DLC 6.1 divided by the response of DLC 1.6.

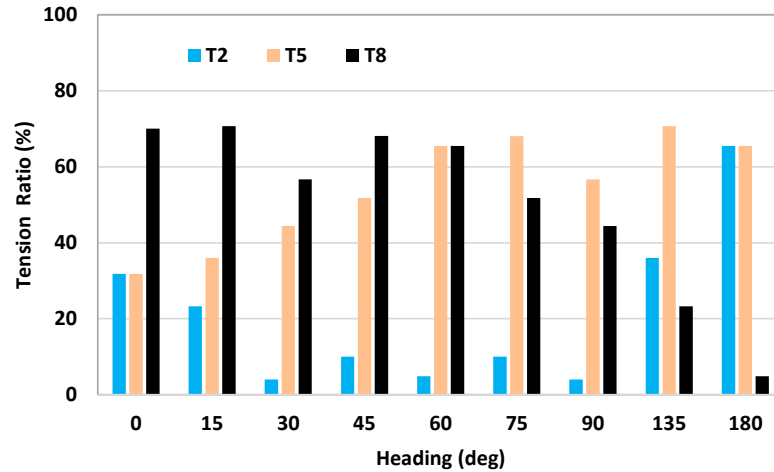


Figure 27. Minimum tension ratio to the pretension at the tendons’ bottom (anchor) for DLC 6.1.

Figure 28a shows the response ratios of the surge, heave, and pitch. The sway, roll, and yaw are excluded in the comparisons, because they are negligibly small for DLC 6.1 under the heading of 0 deg. The ratio of the surge and heave for DLC 6.1 are greater than 1.0, indicating these motions are larger than those for the turbine’s operation. On the other hand, the pitch ratios become smaller than 1.0, meaning that the pitch via the turbine loads is greater than the pitch induced by the environment for DLC 6.1.

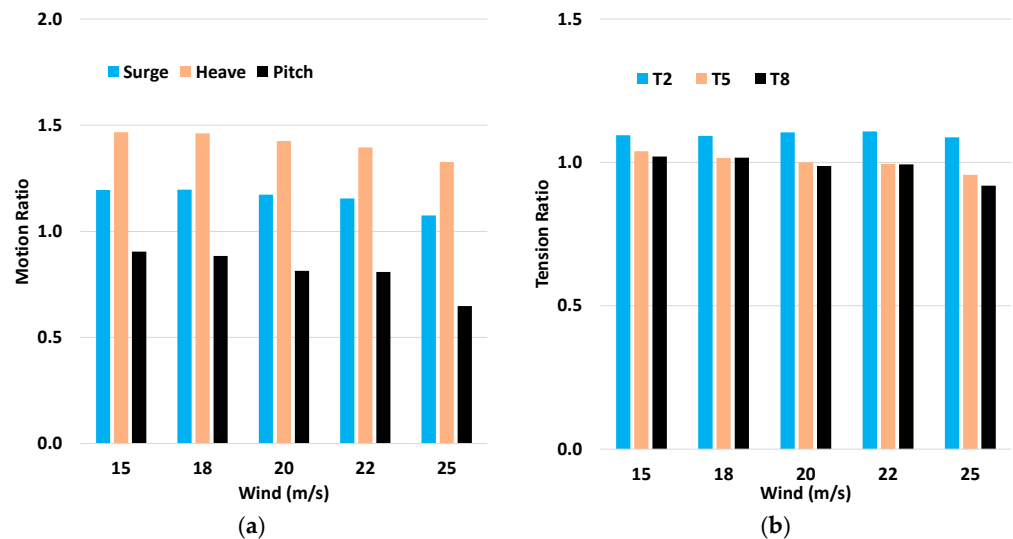
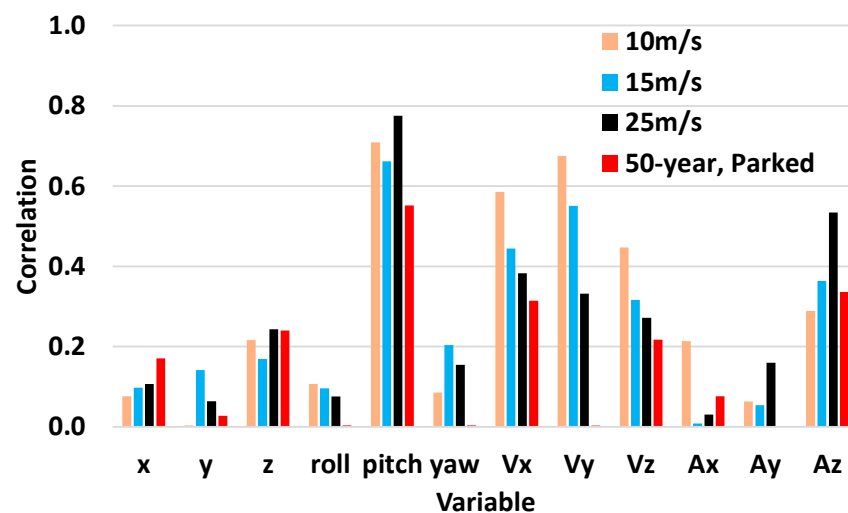


Figure 28. 50-year extreme motion and tension ratio relative to values from DLC1.6: (a) Surge, heave, and pitch ratio; (b) Tension ratio of T2, T5, and T8.

Figure 28b compares the tendon tension ratios of T2, T5, and T8. Considering their environments, T8 is the most loaded tendon and T5 is the next. Therefore, our focus is on T8. The tension ratios for T8 are comparable between DLC 6.1 and DLC 1.6 up to a wind speed of 22 m/s. But at the cut-out wind speed, the ratio falls under 1.0 as such the tension of T8 due to the turbine exceeds the tensions from DLC 6.1. Therefore, it is suggested that a special focus shall be made on the cut-out wind or near the cut-out wind in assessing the tendon strength. These implicate a TLP with a VAWT in the tendon mooring system analysis, which is not commonly observed in a TLP with a HAWT.

#### 4.7. Tendon Tension Correlation

The tendon T8 which is the most loaded tendon among the weatherside tendons is selected to investigate the correlation variables associated with the T8 tension. Both the conditions of DLC 1.6 and DLC 6.1 are considered. For DLC 1.6, wind speeds of 10 m/s, 15 m/s (rated), and 25 m/s (cut-out) are selected. Figure 29 shows the Pearson's correlations of the T8 tension with respect to the variables. The correlation coefficients are computed using an Excel function. The variables  $x$ ,  $y$ , and  $z$  are the tendons' top displacements; the roll, pitch, and yaw are the platform motions;  $V_x$ ,  $V_y$ , and  $V_z$  are the velocities in  $x$ ,  $y$ , and  $z$  directions at the tendons' tops; and  $A_x$ ,  $A_y$ , and  $A_z$  are the accelerations in  $x$ ,  $y$ , and  $z$  directions at the tendons' tops. High correlations (0.66~0.78) are seen in the pitch among the variables at the cut-out wind speed. The velocities ( $V_x$ ,  $V_y$ ,  $V_z$ ) have a higher correlation at the wind speeds of 10 m/s and 15 m/s than the vertical acceleration, while at the cut-out wind speed of 25 m/s, the vertical acceleration shows a higher correlation than the velocities. The vertical displacement ( $z$ ) has a much weaker correlation compared to the vertical velocity ( $V_z$ ) or acceleration ( $A_z$ ). A further analysis finds that the platform pitch at the cut-out wind speed is correlated with the tower base bending moment ( $M_y$ ) and waves.



**Figure 29.** T8 tendon's top tension correlation with respect to variables for the turbine's operation (the combination of the wind-waves at the wind speeds of 10 m/s, 15 m/s, and 25 m/s), and 50-year extreme parked conditions.

For the DLC 6.1 parked turbine (50-year), the T8 tension is also correlated with the platform pitch among other variables. The results for DLC 6.1 show very similar trends to those of DLC 1.6.

#### 4.8. Tendon Fatigue Life Assessment

The original scattered diagram is condensed to a total of 27 fatigue bins, as depicted in Figure 30, in which the wind speeds associated with the bin numbers are also specified. The VAWT turbine is in operation from bin 4 (cut-in) to bin 24 (cut-out) and parked for the other bin conditions. The environments of the wind, waves, and currents are considered. The empirical cumulative probability distribution of the wind is presented in Figure 30. The waves and currents associated with the winds are also shown. Since the directionality of the environment is not defined, three co-directional headings of 0, 45, and 90 deg are considered to identify the heading causing the worst damage to the tendon. A one-hour simulation is run for each bin.

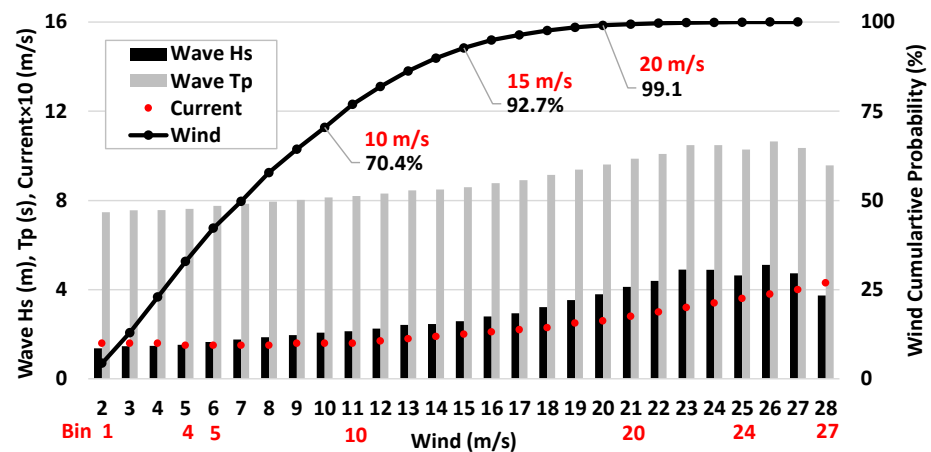


Figure 30. Site scatter diagram for the tendon fatigue assessment.

The tension cycle T-N curve given in Equation (11) can be used to calculate the fatigue lives of the tendons as follows [45].

$$NR^M = K, \tag{11}$$

where  $N$  is the number of cycles, and  $R$  is the ratio of the tension range to the minimum breaking load. For the tendon material of the spiral strand wire rope, the slope  $M$  and intercept  $K$  values in the curve are 5.05 and 166, respectively. The fatigue life is estimated using  $1/D$ , where  $D$  is the annual fatigue damage. The annual damage  $D$  can be calculated from Miner’s rule given as follows:

$$D = \sum \frac{n_i}{N_i}, \tag{12}$$

where  $n_i$  = the number of cycles per year within the tension range interval  $I$ , and  $N_i$  = the number of cycles to failure at the tension range  $I$  as given by the T-N curve.

The fatigue damage is simulated with two different bin settings: the turbine’s operating and parked conditions. The turbine operating bins from bin 4 to 24 consider the turbine loads and environmental loads together. But the turbine is assumed to be parked for the bins out of the turbine’s operation so that only the environmental loads are considered.

The fatigue assessment results are shown In Figure 31 for each heading of 0, 45, and 90 deg. The tendon group of T1, T2, and T3 have a small tendon life in the heading of 90 deg. The lowest life estimated is 144 years for T1 at the heading of 90 deg. The lowest fatigue life is, however, greater than the required minimum of 40 years, based on a platform service life of 20 years and a fatigue design factor (FDF) of 2 for the redundant mooring system specified in [33].

The worst heading of 90 deg is selected and further fatigue assessments are conducted to investigate the load components contributing to the damage to the tendons of T1, T2, and T3. Figure 32a shows the damage per year due to the individual turbine load only (thrust, lateral force, and torque), and the turbine combined which includes all the turbine loads. The turbine-only case considers the bins from bin 4 to bin 24, excluding the wave and current. It is shown that among the turbine load components, the thrusts cause the highest damage to the tendons from T1 to T6. The damage to these tendons by the lateral force and torques are very small. The combined damages to the tendons of T1, T2 and T3 are roughly doubled from the damages by the thrust.

Figure 32b compares the damages due to the turbine combined, the environment only, and all (turbine and environment) combined. The environment-only damages are calculated from the simulations of bin 1 to bin 27 without the turbine’s operation. The damages for all combined and turbine-only cases are from the results in Figures 31c and 32a, respectively. The turbine combined damages are found to be relatively small, compared to

the damages by the environments. However, the total damages to T1, T2, and T3 for all combinations show large increases from those of the turbine combined. The results indicate that the turbine can cause considerable damage to the tendons when they are coupled with the effects of the environment.

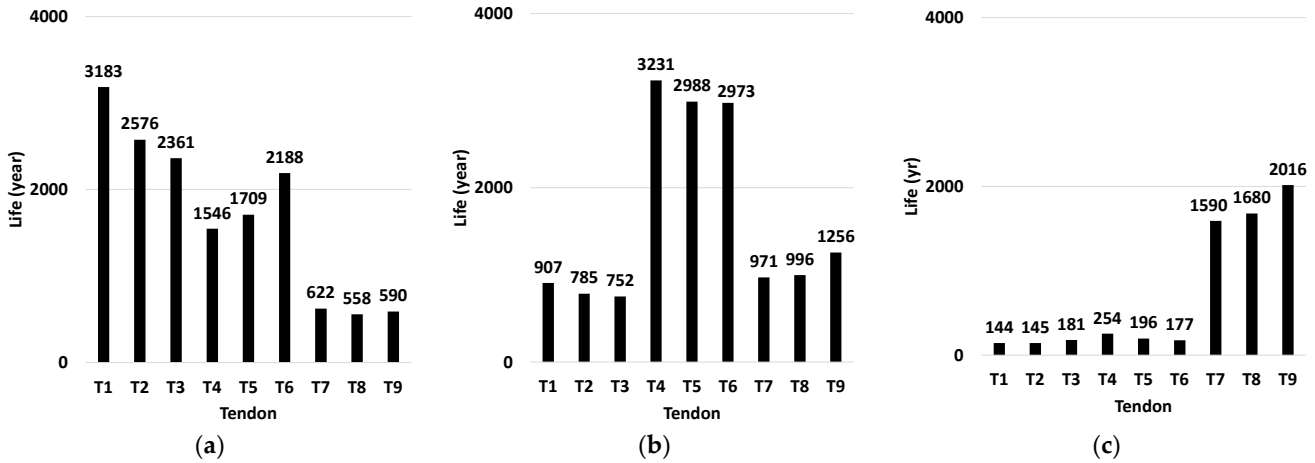


Figure 31. Tendon fatigue lives for the various headings: (a) Heading of 0 deg; (b) Heading of 45 deg; and (c) Heading of 90 deg.

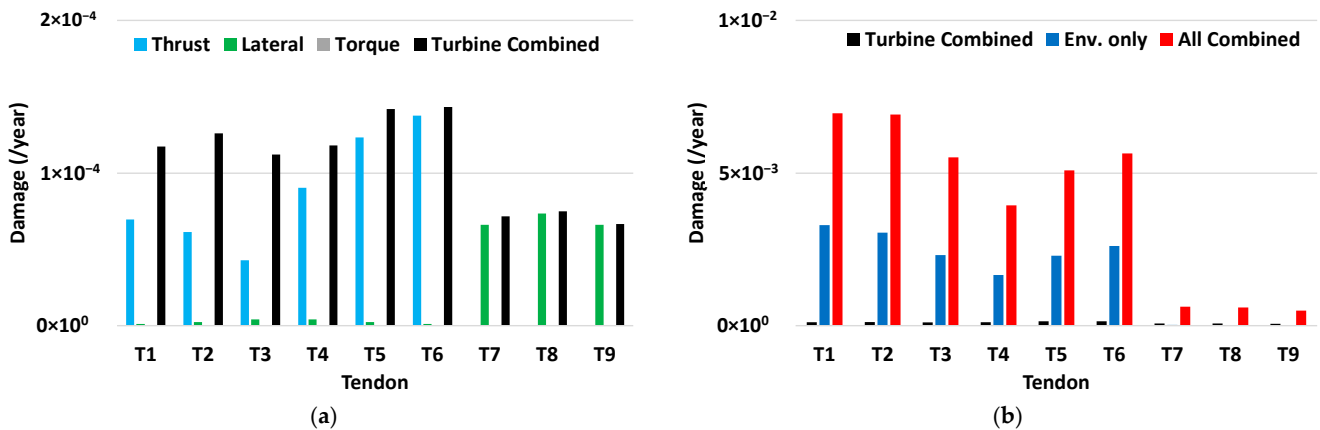


Figure 32. Tendon fatigue damages for the heading of 90 deg: (a) Damages by the turbine load components; (b) Damages by the turbine and environment.

### 5. Conclusions

The modular floating wind platform MarsVAWT TLP is designed to support a 10 MW Darrieus VAWT. The modular foundation consists of multiple modules to overcome the infrastructure limits of yard space, fabrication capacity, and assembly. Modular fabrication allows for floating or onshore assembly, which reduces the assembly and loadout time significantly. The tower’s assembled platform is self-stable, enabling tow-out from quayside. The platform is configured with a total of nine high-pretensioned wire rope tendons to withstand the operating and extreme loads in an offshore site in the Northeast US.

A dynamic response analysis on the MarsVAWT platform is conducted in the time domain with a semi-coupled method, under the severe sea state condition of DLC 1.6 (power production) and 50-year extreme conditions of DLC 6.1 (parked turbine). The response analysis results are as summarized below.

- The tower base maximum shear forces and bending moments are considerably increased under the conditions of the combination of the wind–waves from the wind only, which may suggest the tower’s design should consider the effects of the platform’s motion in waves.

- Due to the inherent VAWT characteristics of high cyclic lateral force and torque values, non-zero mean motions for the sway, roll, and yaw occur over the operating wind ranges.
- The turbine-induced (wind only) dynamic motions of the platform are much smaller than those induced by the waves only.
- The condition for the cut-out wind among the operating winds creates the largest tower base loads, platform motions, and tendon tension, indicating the platform and tendon design need to consider the turbine's operating conditions near the cut-out.
- The tendon tension increases are highly correlated to the platform pitch, as well as the horizontal and vertical velocities and vertical acceleration at the tendon porch.
- Among the turbine load components, the turbine thrust is the most dominant component affecting the tendon tension increase. The torque's contribution to the dynamic tension is very small.
- Tendon tensions on the weatherside at high wind speeds in the range of the rated to the cut-out speeds are comparable to the values under the 50-year extreme (parked). This suggests that the tendon analysis should be conducted to identify the most influential design load cases with more emphasis on both the turbine's operating and extreme parked conditions.
- The platform motion natural frequencies are far off from the turbine excitation and tower mode frequencies, except for the pitch (and roll) which are close to the turbine 6P.
- The turbine excitations of 3P and 6P as well as the tower mode frequency effects are strongly present in the associated response PSDs of the tower base loads (shear force, bending moment), platform pitch, and tendon tension.
- As for DLC 6.1, the maximum tendon tension is observed in an environment heading of 90 deg, which shows the heading's dependency on the tension. The extreme tension is roughly 1.5 to 2 times more than the pretension, depending on the environment heading.
- The minimum tendon tension simulated is a small positive value. Although the result passes the design requirements for a positive tension, additional analyses are suggested to confirm this further.
- The combined tendon fatigue damage from the turbine and the environment is significantly higher than that from the environment only or the turbine only, showing a high coupling effect to the tendon damage when coupled.
- Among the turbine load components, the thrust contributes more to the tendon fatigue damage.
- The assessment results of the tendon strength and fatigue designs confirm the tendon design complies with the design requirements of industry standards.

The MarsVAWT TLP with a 10 MW VAWT was designed and confirmed to comply with industry standards and practices. In this paper, details about its performance are provided to show a potential solution for large-scale floating wind turbines.

**Author Contributions:** Conceptualization, S.Y.B. and S.A.S.; methodology, S.Y.B.; software, S.Y.B.; validation, S.Y.B., D.T.G. and A.S.E.M.; formal analysis, S.Y.B.; investigation, S.A.S.; resources, S.Y.B. and S.A.S.; data curation, S.Y.B., D.T.G. and A.S.E.M.; writing—original draft preparation, S.Y.B.; writing—review and editing, S.A.S., D.T.G. and A.S.E.M.; visualization, S.Y.B.; supervision, S.A.S.; project administration, S.A.S.; funding acquisition, D.T.G. All authors have read and agreed to the published version of the manuscript.

**Funding:** The present work was funded by the US Department of Energy Advanced Research Projects Agency-Energy (ARPAE) under the ATLANTIS program with project title "A Low-cost Floating Offshore Vertical Axis Wind System" with Award No. DE-AR0001179. Any opinions, findings, and conclusions or recommendations expressed in this material are those of the authors and do not necessarily reflect the views of ARPA-E.

**Institutional Review Board Statement:** Not applicable.

**Informed Consent Statement:** Not applicable.

**Data Availability Statement:** Not applicable.

**Conflicts of Interest:** The authors declare no conflict of interest.

### Abbreviations

The following abbreviations are used in this manuscript:

ARPA-E	Advanced Research Projects Agency–Energy
ATLANTIS	Aerodynamic Turbines Lighter and Afloat with Nautical Technologies and Integrated Servo-control
CACTUS	Code for Axial and Cross-flow Turbine Simulation
CoG	Center of Gravity
DAF	Dynamic Amplification Factor
DLC	Design Load Case
DoE	Department of Energy
FDF	Fatigue Design Factor
FoS	Factor of Safety
HAWT	Horizontal Axis Wind Turbine
JONSWAP	Joint North Sea Wave Observation Project
MARS	Modular Assembly and Reconfigurable System
MW	Megawatt
MBL	Minimum Breaking Load
NREL	National Renewable Energy Laboratory
NPD	Norwegian Petroleum Directorate
OWENS	Offshore Wind ENergy Simulation toolkit
PC	Pressure Center
PSD	Power Spectral Density
RAO	Response Amplitude Operator
SWL	Still Water Line
T-N	Tension-Cycle
TLP	Tension Leg Platform
VAWT	Vertical-Axis Wind Turbine

### References

- Jonkman, J.M.; Butterfield, S.; Musial, W.; Scott, G. *Definition of a 5-MW Reference Wind Turbine for Offshore System Development*; Technical Report NREL/TP-500-38060; National Renewable Energy Laboratory: Golden, CO, USA, 2009.
- Jonkman, J.M. Dynamics of Offshore Floating Wind Turbines—Model development and Verification. *Wind Energy* **2009**, *12*, 459–492. [CrossRef]
- Gaertner, E.; Rinker, J.; Sethuraman, L.; Zahle, F.; Anderson, B.; Barter, G.; Abbas, N.; Meng, F.; Bortolotti, P.; Skrzypinski, W.; et al. *IEA Wind TCP Task 37: Definition of the IEA Wind 15-Megawatt Offshore Reference Wind Turbine*; National Renewable Energy Laboratory: Golden, CO, USA, 2020; NREL/TP-5000-75698. Available online: <https://www.nrel.gov/docs/fy20osti/75698.pdf> (accessed on 12 August 2023).
- Allen, C.; Viselli, A.; Dagher, H.; Goupee, A.; Gaertner, E.; Abbas, N.; Hall, M.; Barter, G. *Definition of the UMaine VoltturnUS-S Reference Platform Developed for the IEA Wind 15-Megawatt Offshore Reference Wind Turbine*; Technical Report; National Renewable Energy Laboratory: Golden, CO, USA, 2020.
- Liu, Y.; Hu, C.; Sueyoshi, M. Motion Response Characteristics of a Kyushu-University Semi-Submersible Floating Wind Turbine with Trussed Slender Structures: Experiment vs. Numerical Simulation. *Ocean Eng.* **2021**, *232*, 109078. [CrossRef]
- TwindWind. Available online: <https://hexiconpower.com/twinwind/> (accessed on 12 August 2023).
- American Bureau of Shipping (ABS). ABS ClaYoshida, Shigeosses World’s Biggest Floating Wind Turbine. Available online: <https://ww2.eagle.org/en/news/press-room/abs-classes-worlds-biggest-floating-wind-turbine.html> (accessed on 12 August 2023).
- Equinor, Hywind Scotland. Available online: <https://www.equinor.com/energy/hywind-scotland>. (accessed on 12 August 2023).
- Arredondo-Galeana, A.; Brennan, F. Floating Offshore Vertical Axis Wind Turbines: Opportunities, Challenges and Way Forward. *Energies* **2021**, *14*, 8000. [CrossRef]
- Tjiu, W.; Marnoto, T.; Mat, S.; Ruslan, M.H.; Sopian, K. Darrieus vertical axis wind turbine for power generation I: Assessment of Darrieus VAWT configurations. *Renew. Energy* **2015**, *75*, 50–67. [CrossRef]
- Kumar, P.M.; Sivalingam, K.; Teik-Cheng Lim, T.-C.; Ramakrishna, S.; Wei, H. Review on the Evolution of Darrieus Vertical Axis Wind Turbine: Large Wind Turbines. *Clean Technol.* **2019**, *1*, 205–223. [CrossRef]

12. Griffith, D.T.; Barone, M.; Paquette, J.; Owens, B.; Bull, D.; Simao-Ferreira, C.; Goupee, A.J.; Fowler, M.J. *Design Studies for Deep-Water Floating Offshore Vertical Axis Wind Turbines*; Technical Report, SAND2018-7002; Sandia National Laboratories: Albuquerque, NM, USA, 2018.
13. Gharaati, M.; Xiao, S.; Wei, N.J.; Martínez-Tossas, L.A.; Dabiri, J.O.; Yang, D. Large Eddy Simulation of Helical- and Straight-Bladed Vertical Axis Wind Turbines in Boundary Layer Turbulence. *J. Renew. Sustain. Energy* **2022**, *14*, 053301. [[CrossRef](#)]
14. Whittlesey, R.W.; Liska, S.; Dabiri, J.O. Fish schooling as a basis for vertical axis wind turbine farm design. *Bioinspir. Biomim.* **2010**, *5*, 3. [[CrossRef](#)]
15. Sakib, M.S.; Griffith, D.T. Parked and operating load analysis in the aerodynamic design of multi-megawatt-scale floating vertical-axis wind turbines. *Wind Energy Sci.* **2022**, *7*, 677–696. [[CrossRef](#)]
16. Gao, J.; Griffith, T.D.; Sakib, M.S.; Boo, S.Y. A semi-coupled aero-servo-hydro numerical model for floating vertical axis wind turbines operating on TLPs. *Renew. Energy* **2022**, *181*, 692–713. [[CrossRef](#)]
17. Galinos, C.; Larsen, T.J.; Madsen, H.A.; Paulsen, U.S. Vertical axis wind turbine design load cases investigation and comparison with horizontal axis wind turbine. In Proceedings of the 13th Deep Sea Offshore Wind R&D Conference, Trondheim, Norway, 20–22 January 2016.
18. Huijs, F.; Vlasveld, E.; Gormand, M.; Savenije, F.; Caboni, M.; LeBlanc, B.; Ferreira, C.S.; Lindenburg, K.; Gueydon, S.; Otto, W.; et al. Integrated design of a semi-submersible floating vertical axis wind turbine (VAWT) with active blade pitch control. In Proceedings of the EERA DeepWind'2018, 15th Deep Sea Offshore Wind R&D Conference, Trondheim, Norway, 17–19 January 2018.
19. Wen, T.R.; Wang, K.; Cheng, Z.; Ong, M.C. Spar-Type Vertical-Axis Wind Turbines in Moderate Water Depth: A Feasibility Study. *Energies* **2018**, *11*, 555. [[CrossRef](#)]
20. Berthelsen, P.A.; Fylling, I.; Vita, L.; Paulsen, U.S. Conceptual Design of a Floating Support Structure and Mooring System for a Vertical Axis Wind Turbine. In Proceedings of the ASME 2012 31st International Conference on Ocean, Offshore and Arctic Engineering OMAE2012, Rio de Janeiro, Brazil, 1–6 July 2012.
21. SeaTwirl. 1-MW Floating Vertical Axis Wind Turbine to Be Deployed off Norway. Available online: <https://newatlas.com/energy/seatwirl-vawt-norway/> (accessed on 12 August 2023).
22. Ishie, J.; Wang, K.; Ong, M.C. Structural Dynamic Analysis of Semi-Submersible Floating Vertical Axis Wind Turbines. *Energies* **2016**, *9*, 1047. [[CrossRef](#)]
23. Wang, K.; Moan, T. A Method of Floating Vertical Axis Wind Turbine. In Proceedings of the ASME 2013 32nd International Conference on Ocean, Offshore and Arctic Engineering OMAE2013, Nantes, France, 9–14 June 2013.
24. Robertson, A.; Jonkman, J.; Masciola, M.; Song, H.; Goupee, A.; Coulling, A.; Luan, C. *Definition of the Semisubmersible Floating System for Phase II of OC4*; National Renewable Energy Laboratory: Golden, CO, USA, 2012.
25. VERTIWIND. Offshore Floating Vertical Axis Wind Turbine. Available online: <https://www.epsilon-composite.com/en/case-study/vertiwind-vertical-axis-wind-turbine> (accessed on 12 August 2023).
26. Withee, J. Fully Coupled Dynamic Analysis of a Floating Wind Turbine System. Ph.D. Thesis, Department of Ocean Engineering, Massachusetts Institute of Technology, Cambridge, MA, USA, 2004.
27. Robertson, A.N.; Jonkman, J.M. Loads Analysis of Several Offshore Floating Wind Turbine Concepts. In Proceedings of the Twenty-First International Offshore and Polar Engineering Conference, Maui, HI, USA, 19–24 June 2011.
28. Erin, E.; Bachynski, E.E.; Moan, M. Design considerations for tension leg platform wind turbines. *Mar. Struct.* **2012**, *29*, 89–114.
29. Boo, S.Y.; Shelley, A.S.; Kim, D. A TLP Floating Foundation Design with Novel Tendon Mooring Technology for Hawaii Offshore Wind. In Proceedings of the Twenty-Ninth International Ocean and Polar Engineering Conference, Honolulu, HI, USA, 16–21 June 2019.
30. Adam, F.; Myland, T.; Dahlhaus, F.; Großmann, J. GICON-TLP for wind turbines—The path of development. In Proceedings of the 1st International Conference on Renewable Energies Offshore (RENEW), Lisbon, Portugal, 24–26 November 2014.
31. Li, Y.; Le, C.; Ding, H.; Zhang, P.; Zhang, J. Dynamic Response for a Submerged Floating offshore Wind Turbine with Different Mooring Configurations. *J. Mar. Sci. Eng.* **2019**, *7*, 115. [[CrossRef](#)]
32. Borg, M.; Collu, M. Offshore floating vertical axis wind turbines, dynamics modelling state of the art. Part III: Hydrodynamics and coupled modelling approaches. *Renew. Sustain. Energy Rev.* **2015**, *46*, 296–310. [[CrossRef](#)]
33. American Bureau of Shipping (ABS). *ABS Guide for Building and Classing Floating Offshore Wind Turbines*; American Bureau of Shipping: Houston, TX, USA, 2020.
34. American Petroleum Institute (API). *API RP 2T Planning, Designing, and Constructing Tension Leg Platform*; American Petroleum Institute: Washington, DC, USA, 2010.
35. OrcaFlex—Dynamic Analysis Software for Offshore Marine Systems. Available online: <https://www.orcina.com/orcaflex/> (accessed on 12 August 2023).
36. ARPA-E. Advanced Research Projects Agency–Energy. Available online: <https://arpa-e.energy.gov/technologies/projects/low-cost-floating-offshore-vertical-axis-wind-system> (accessed on 12 August 2023).
37. Hsu, W.-T.; Litton, R.; Vasala, H.; Anderson, D.; Sheppard, R. Beneficial Wave Motion Response for Wind Turbine Support TLPs with Synthetic Rope Tendons. In Proceedings of the Offshore Technology Conference, Houston, TX, USA, 6–9 May 2019.

38. Murray, J.C.; Barone, M. The development of CACTUS, a wind and marine turbine performance simulation code. In Proceedings of the 49th AIAA Aerospace Sciences Meeting Including the New Horizons Forum and Aerospace Exposition, Orlando, FL, USA, 4–7 January 2011.
39. Viselli, A.; Forristall, G.; Dagher, H. Estimation of extreme wave and wind design parameters for offshore wind turbines in the Gulf of Maine using a POT method. *Ocean Eng.* **2015**, *104*, 649–658. [[CrossRef](#)]
40. American Bureau of Shipping (ABS). *ABS Rules for Building and Classing Floating Production Installations*; American Bureau of Shipping: Houston, TX, USA, 2014.
41. Owens, B.C. Theoretical Developments and Practical Aspects of Dynamic Systems in Wind Energy Application. Ph.D. Dissertation, Department of Aerospace Engineering, Texas A&M University, College Station, TX, USA, 2013.
42. Wehmeyer, C.; Ferri, F.; Andersen, M.T.; Pedersen, R.R. Hybrid Model Representation of a TLP Including Flexible Topsides in Non-Linear Regular Waves. *Energies* **2014**, *7*, 5047–5064. [[CrossRef](#)]
43. Gueydon, S.; Jonkman, J. Update on the Comparison of Second-Order Loads on a Tension Leg Platform for Wind Turbines. In Proceedings of the Twenty-Sixth International Ocean and Polar Engineering Conference (ISOPE), Rhodes, Greece, 26 June–1 July 2016.
44. Det Norske Veritas (DNV). *DNVGL-OTG-13, Offshore Technical Guidance*; Det Norske Veritas (DNV): Høvik, Norway, 2019.
45. American Petroleum Institute (API). *API RP 2SK Design and Analysis of Stationkeeping Systems for Floating Structures*; American Petroleum Institute: Washington, DC, USA, 2005.

**Disclaimer/Publisher’s Note:** The statements, opinions and data contained in all publications are solely those of the individual author(s) and contributor(s) and not of MDPI and/or the editor(s). MDPI and/or the editor(s) disclaim responsibility for any injury to people or property resulting from any ideas, methods, instructions or products referred to in the content.